

Precipitation Susceptibility and Aerosol Buffering of Warm- and Mixed-Phase Orographic Clouds in Idealized Simulations

FRANZISKA GLASSMEIER^a AND ULRIKE LOHMANN

Institute for Atmospheric and Climate Science, ETH Zürich, Zurich, Switzerland

(Manuscript received 24 August 2017, in final form 4 January 2018)

ABSTRACT

The sensitivity of warm- and mixed-phase orographic precipitation to the aerosol background with simultaneous changes in the abundance of cloud condensation nuclei and ice nucleating particles is explored in an idealized, two-dimensional modeling study. The concept of precipitation susceptibility $d\ln P/d\ln N$, where P is the precipitation mixing ratio and N the cloud droplet number, is adapted for orographic clouds. Precipitation susceptibility is found to be low because perturbations to different precipitation formation pathways compensate each other. For mixed-phase conditions, this in particular means a redistribution between warm and cold pathways. The compensating behavior is described as a consequence of a balance equation for the cloud water along parcel trajectories that constrains the total precipitation formation to match the drying from condensation and vapor deposition on ice-phase hydrometeors caused by the mountain flow. For an aerosol-independent condensation rate (saturation adjustment), this balance requirement limits aerosol impacts on orographic precipitation (i) to the evaporation of hydrometeors and (ii) to the glaciation state of the cloud, which controls the contribution of vapor deposition to drying. The redistribution of precipitation formation pathways is coupled to a redistribution of the total hydrometeor mass between hydrometeor categories. Aerosol effects on the glaciation state of the cloud enhance this redistribution effect such that liquid and ice adjustments do not compensate. For the externally constrained, fully adjusted steady-state situation studied, precipitation susceptibility quantifies the redistribution effect rather than changes in precipitation production as in previous studies.

1. Introduction

Orographic clouds are especially prone to exhibit aerosol–cloud–precipitation interactions because the mountain flow limits the time available for precipitation formation. By controlling the time scale at which small cloud hydrometeors are converted into precipitation hydrometeors, aerosol perturbations can shift the horizontal locations where hydrometeor types occur. Shifting the location of precipitation controls the leeward-precipitation fraction (spillover factor); shifting

the location of small hydrometeors affects the extent of reevaporation (drying ratio). Aerosol effects on orographic precipitation are typically studied either in the context of deliberate cloud seeding, where the abundance of ice-formation aerosol [ice nucleating particles (INPs)] is increased (e.g., Xue et al. 2013; Geresdi et al. 2017), or in the context of anthropogenic pollution, which is usually assumed to be represented by an increase in cloud droplet-forming aerosol [cloud condensation nuclei (CCN); e.g., Saleeby et al. 2009, 2011]. For warm orographic clouds, increases in CCN lead to more but smaller cloud droplets, which decrease the autoconversion efficiency and thus lead to a delay in precipitation formation, equivalent to the mechanism discussed by Albrecht (1989) for shallow maritime clouds. Miltenberger et al. (2015) showed that the warm orographic precipitation efficiency, defined as the fraction of cloud water that is converted into precipitation, scales with the ratio of an advective time scale and a time scale of microphysical conversion, which is influenced by the

 Denotes content that is immediately available upon publication as open access.

^a Current affiliation: Chemical Sciences Division, NOAA/Earth System Research Laboratory, Boulder, Colorado.

Corresponding author: Franziska Glassmeier, franziska.glassmeier@noaa.gov

DOI: 10.1175/JAS-D-17-0254.1

© 2018 American Meteorological Society. For information regarding reuse of this content and general copyright information, consult the [AMS Copyright Policy](https://www.ametsoc.org/PUBSReuseLicenses) (www.ametsoc.org/PUBSReuseLicenses).

abundance of CCN. According to this scaling relationship, precipitation efficiency increases for decreasing droplet, or CCN, numbers for low and intermediate precipitation efficiencies. At high precipitation efficiencies, where the time for precipitation formation is always sufficiently long, the aerosol effect levels off.

In polluted mixed-phase clouds, the slowing effect of decreased droplet size on autoconversion is replaced by a slowing effect on riming (Borys et al. 2003). The corresponding delay in precipitation formation and spillover effect is found to be enhanced by the slower fall speeds and longer vertical trajectories of lightly rimed ice (Saleeby et al. 2009, 2011). Although it is statistically difficult to assess the success of deliberate cloud seeding of orographic clouds with INPs in the field (Chu et al. 2017), modeling studies generally find precipitation enhancement for stratiform clouds. Increased depletion of the water vapor (increased drying) by diffusional growth of ice-phase hydrometeors has been identified as the most important contribution to precipitation enhancement (Xue et al. 2013; Geresdi et al. 2017). Similar to the warm case, seeding is found to be less efficient for higher precipitation efficiencies in these studies.

In general, perturbations to the liquid- and ice-phase pathways to precipitation formation cannot be discussed separately. Atmospheric aerosol usually provides CCN and INPs simultaneously, and the interaction of liquid and ice microphysics is the very essence of mixed-phase clouds. As discussed, INPs and the ice-phase pathway of vapor deposition tend to accelerate and increase precipitation formation, while CCN and droplet-collection processes like autoconversion and riming are associated with fewer and later precipitation formation. In accordance with this complementary behavior, the response of mixed-phase clouds to simultaneous CCN and INP perturbations has been found of inconclusive sign and is in general small (Muhlbauer et al. 2010). Next to the opposing effects of CCN and INP perturbations, the complexity of mixed-phase cloud microphysics itself predisposes compensating responses of different processes to aerosol perturbations and buffering behavior (Glassmeier and Lohmann 2016).

This study aims to clarify how different pathways to precipitation formation interact in their response to aerosol perturbations and identify orographic controls of this interplay. In our approach, we adapt the concept of precipitation susceptibility to orographic clouds. In its original form (Feingold and Siebert 2009), precipitation susceptibility s is a vertically averaged concept and quantifies the relative change $d\ln R = dR/R \approx \Delta R/R$ in warm rain rate R that follows from a relative change in

cloud droplet number concentration N_{cl} (Feingold and Siebert 2009),¹

$$s = \frac{d\ln R}{d\ln N_{cl}} = \left. \frac{\partial \ln R}{\partial \ln N_{cl}} \right|_{LWP} + \left. \frac{\partial \ln R}{\partial \ln LWP} \right|_{N_{cl}} \frac{d\ln LWP}{d\ln N_{cl}}, \quad (1)$$

such that the numerical value of s indicates the percentage change in R that follows from a 1% change in N_{cl} . The right-hand side of Eq. (1) separates the total precipitation susceptibility into the partial precipitation susceptibility when fixing the liquid water path (LWP; indicated by $|_{LWP}$) and the secondary effect, or *adjustment*, of changes in LWP that are typically triggered by a perturbation in N_{cl} . Precipitation susceptibility is usually interpreted in relation to the sensitivities of microphysical conversion rates. For global models with diagnostic precipitation, precipitation susceptibility corresponds to the autoconversion exponent (Stevens and Feingold 2009). For prognostic precipitation, precipitation susceptibility decreases as warm rain formation transitions from droplet-number-dependent autoconversion to droplet-number-independent accretion (at fixed liquid water content; Sorooshian et al. 2009; Wood et al. 2009; Glassmeier and Lohmann 2016). If aerosol perturbations do not trigger adjustments in the amount of cloud ice (i.e., the glaciation state of the cloud), mixed-phase clouds are expected to feature lower precipitation susceptibilities than warm clouds. This is a consequence of the compensations discussed above and of riming not being as sensitive to changes in droplet number as autoconversion (Glassmeier and Lohmann 2016). Strong precipitation susceptibilities in mixed-phase clouds can be observed when the aerosol perturbation triggers glaciation adjustments (Glassmeier and Lohmann 2016). Precipitation susceptibility can thus qualitatively capture the sensitivities of precipitation efficiency to aerosol perturbations.

The intuitive arguments above are based on the assumption that precipitation susceptibility s is dominated by the first term on the right-hand side of Eq. (1). As adjustments require time to respond to the perturbation, this assumption is expected to be justified on a short time scale after a perturbation. In contrast, orographic clouds can be idealized as steady-state systems that have fully adjusted to applied perturbations. These adjustments can lead to counterintuitive sensitivities. For an illustration, consider a box model of a cloud in which cloud water C is created by condensation (cond) and converted with a parameter α into precipitation hydrometeors P , which are depleted by sedimentation with a sedimentation velocity σ :

¹ We have omitted the conventional minus sign in our definition of precipitation susceptibility because this minus was motivated by the use for warm clouds.

$$\dot{C} = \text{cond} - \alpha CP, \quad (2)$$

$$\dot{P} = -\sigma P + \alpha CP. \quad (3)$$

The steady-state solution $\dot{C} = \dot{P} = 0$ of this system is $C = \sigma/\alpha$, $P = \text{cond}/\sigma$. A decrease in the background aerosol corresponds to an increase of α . On the short time scale, Eq. (3) indicates an increase in P for increasing α . When the system has readjusted to a steady state, P will have the same value that it had before the perturbation. More realistic versions of such box models that especially take into account nonlinear conversion rates from C to P have been discussed by Wacker (1995, 2006) and Jiang and Smith (2003).

In this study, we will probe orographic precipitation susceptibility by performing idealized two-dimensional simulations of warm- and mixed-phase orographic clouds for a variety of realistic aerosol conditions. To account for the horizontal, rather than vertical, development of orographic clouds, we base our analysis on parcel trajectories and define precipitation susceptibility for trajectory rather than vertical averages. The parcel perspective allows us to formulate balance equations that formalize the relationship between precipitation susceptibility and the interplay of process rates and provides insights into the role of adjustments. The rest of the paper is organized as follows: In section 2, we describe the numerical model and its setup for this study. The discussion of our results in section 3 starts with a qualitative discussion of aerosol effects on orographic clouds from the trajectory-averaged perspective, continues with implications of the cloud water budget along trajectories, and concludes with the discussion of orographic precipitation susceptibilities. Section 4 provides a discussion and summary of the results. The appendix provides a list of symbols and acronyms.

2. Model and simulations

We use the nonhydrostatic limited-area atmospheric model of the Consortium for Small Scale Modelling (COSMO; Baldauf et al. 2011) in its 2D setup and make use of the Aerosols and Reactive Trace Gases (ART) extension of the model (COSMO-ART; Vogel et al. 2009), which comprises aerosol–cloud interactions based on chemical and physical properties of aerosol populations (Bangert et al. 2011, 2012) with the M7 aerosol scheme (COSMO-ART-M7; Glassmeier et al. 2017). As the present study focuses on the aerosol effect on precipitation formation rather than on activation and freezing, we prescribe measurement-based aerosol fields (section 2b) rather than dynamically calculating its evolution from emissions. Therefore, we disable aerosol microphysical evolution (i.e., condensation, coagulation,

sedimentation, and washout). Aerosol activation follows Fountoukis and Nenes (2005) and is based on a CCN spectrum derived from Köhler theory (Köhler 1936) in combination with a population-splitting approach to solve the supersaturation budget (Nenes and Seinfeld 2003). Improved in-cloud activation is included according to Barahona et al. (2010) by treating existing droplets as giant CCN. Following Glassmeier et al. (2017), we assume immersion freezing to be the sole ice formation process in mixed-phase clouds. We consider dust as immersion INPs using the parameterization of Phillips et al. (2008). Immersion freezing is considered the most important ice formation process (Kanji et al. 2017) for mixed-phase clouds. Deposition nucleation is only important in the absence of liquid water (i.e., for cirrus clouds). Contact nucleation is poorly understood and could potentially be important for mixed-phase clouds under specific conditions (Hande et al. 2017). For the simulated case, the exclusion of contact freezing is no limitation because the case does not feature uncoated INPs, which are required to initiate contact freezing in existing parameterizations. We do not consider ice multiplication. Aerosol is not scavenged by droplet activation. Instead, CCN and INP depletion is implemented as a number adjustment. We employ the two-moment cloud microphysics scheme of Seifert and Beheng (2006, hereafter SB) in the updated version of Noppel et al. (2010) with five hydrometeor classes (cloud water, ice, rain, snow, and graupel). While vapor deposition on ice-phase hydrometeors is explicitly described in the scheme, condensation is implemented by means of a saturation adjustment. This has implications for the Wegener–Bergeron–Findeisen (WBF) process (Wegener 1911; Bergeron 1935; Findeisen 1938), which describes the growth of ice-phase hydrometeors at the expense of cloud droplets because saturation vapor pressure with respect to water is higher than that with respect to ice. The WBF process is technically separated into two steps: First, vapor deposition on ice is calculated, and the corresponding depletion of water vapor leads to subsaturation with respect to water. Later in the time step, the saturation adjustment transfers cloud water to the vapor phase to reach water saturation. Radiation is not considered.

a. Setup

Following Miltenberger et al. (2015), we use a setup with 150 vertical and 750 horizontal grid points at a domain height of 22 km and a horizontal resolution of 1 km. The time step is 6 s. A bell-shaped hill with a maximum height of $h_{\text{max}} = 0.8$ km and a half-width $a = 20$ km is placed in the domain center (cf. Fig. 3). The corresponding orography profile is given by

$$h(d) = \frac{h_{\max}}{1 + (d/a)^2}, \quad (4)$$

where d denotes the horizontal distance from the center.

Our initial and boundary conditions are motivated by [Muhlbauer et al. \(2010\)](#) and are illustrated in [Fig. 1](#). The temperature profile corresponds to a dry Brunt–Väisälä frequency of $N_d = 0.018 \text{ s}^{-1}$ with a surface temperature of $T_s = 296.15 \text{ K}$ for the warm case and $N_d = 0.013 \text{ s}^{-1}$ with $T_s = 270.15 \text{ K}$ for the mixed-phase cloud. The moisture profile is in both cases given by the following expression for the saturation ratio:

$$S(z) = a + \frac{b - a}{1 - \exp[-c(z - z_0)]}, \quad (5)$$

where z denotes the metric height and the parameters take the values $a = 0.95$, $b = 0.03$, $c = 0.0015 \text{ m}^{-1}$, and $z_0 = 6000 \text{ m}$. The wind profile has no updraft component and is vertically constant with a value of 20 m s^{-1} in the analysis region. Above, it increases linearly toward a value of 40 m s^{-1} at the model top.

We run this setup for 50 h. We allow the system to equilibrate for 30 h and base our analysis on 15-min output from the remaining 20 h. We average temporally to obtain steady-state fields.

In the steady-state situation the boundary conditions are chosen to obtain a linear mountain wave [see the updraft profile (black contours) in [Fig. 3](#)] and a stratification that is stable enough to prevent convection. The profiles of equivalent potential temperature θ_e indicate stability ([Cotton and Anthes 1992](#)):

$$\theta_e = T \left(\frac{p_0}{p_d} \right)^{R_d/(c_{pd} + c_l q_t)} \exp \left[\frac{L_v q_v - L_f q_i}{(c_{pd} + c_l q_t) T} \right], \quad (6)$$

where T denotes the temperature; $p_0 = 1000 \text{ hPa}$ the reference pressure; p_d the pressure of dry air; $R_{d/v}$ the gas constants of dry and moist air; $c_{pd/l}$ the heat capacities at constant pressure of dry air and of water; $q_{v/it}$ the mixing ratios of water vapor, ice, and total water; and $L_{v/f}$ the latent heat of vaporization and fusion. While the thermodynamic initial and boundary profiles result in a stable stratification for the mixed-phase cloud, the high surface temperatures of the warm profile result in a slightly unstable stratification, which does not affect the subsequent analysis. The high surface temperatures are necessary to ensure that the cloud top lies at temperatures warmer than the freezing level.

b. Aerosol perturbations

In addition to the dynamic and thermodynamic profiles, an aerosol composition is prescribed at the left

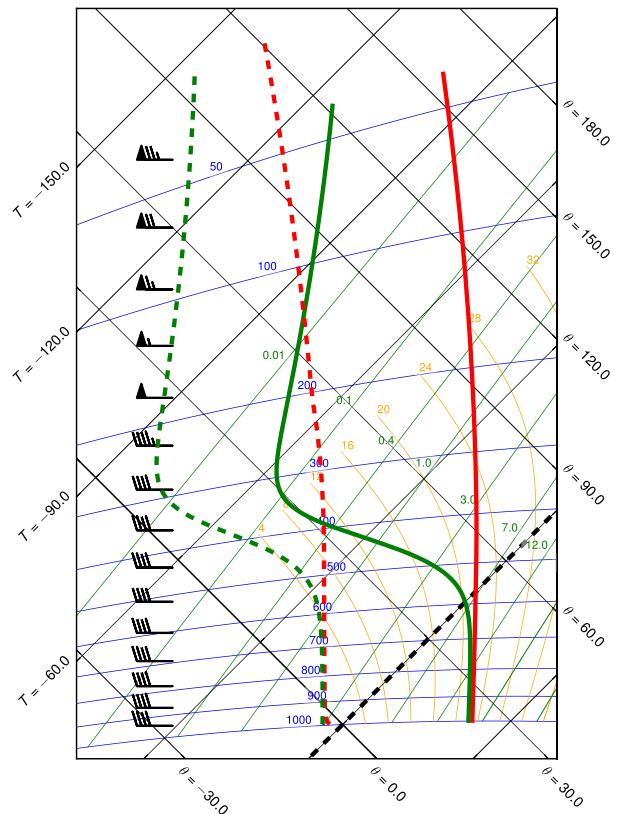


FIG. 1. Initial and boundary conditions. The tephigram shows temperature (red) and dewpoint temperature (green) profiles for the warm (solid lines) and mixed-phase cloud (dashed lines). The black bars indicate the profile of horizontal wind speed that is identical for both cases. Wind speed is constant at a value of 20 m s^{-1} in the analysis region $>300 \text{ hPa}$ and increases toward a value of 40 m s^{-1} at model top.

boundary of the domain. The aerosol composition is fixed but transported with the flow. Following [Muhlbauer et al. \(2010\)](#), we apply a vertically constant aerosol profile based on point measurements from the high-alpine station Jungfraujoch (JFJ) in Switzerland for clean and polluted conditions as summarized in [Table 1](#).

Total aerosol mass and number concentrations have been derived by [Muhlbauer et al. \(2010\)](#) based on measurements from [Weingartner et al. \(1999\)](#). We assume that all aerosol has been coated during transport to the remote location JFJ. Since no significant contribution of the coarse mode to the climatological values was observed and nucleation mode aerosol neither directly nor indirectly affects cloud microphysics in our setup, the relevant aerosol composition is thus described by a coated Aitken and a coated accumulation mode. Similar to [Muhlbauer et al. \(2010\)](#), we base the chemical composition of these modes on [Cozic et al. \(2008\)](#). We assume the following mass ratios of black carbon (BC) to organic carbon (OC) to sulfate (SU) aerosol:

TABLE 1. Measurement-based aerosol conditions for clean and polluted situations based on Muhlbauer et al. (2010) with natural [$f_{\text{SU}} = M_{\text{SU}}/(M_{\text{SU}} + M_{\text{DU}}) = 0.6$] and anthropogenic ($f_{\text{SU}} = 0.9$) partitioning of accumulation-mode sulfate mass M_{SU} and dust mass M_{DU} [cf. Eq. (8)].

Mode	Situation	Number (10^8 m^{-3})	Mass ($\mu\text{g m}^{-3}$)				
			Total	SU	OC	BC	DU
Aitken	Clean–natural	3.1	0.07	0.0287	0.0385	0.0028	—
	Polluted–anthropogenic	5.3	0.26	0.1066	0.1430	0.0104	—
Accumulation	Clean–natural	0.4	0.44	0.1082	0.2420	0.0176	0.0722
	Polluted–anthropogenic	2.6	1.74	0.6421	0.9570	0.0696	0.0713

$$\text{BC}:\text{OC}:\text{SU} = 0.04:0.55:0.41. \quad (7)$$

In the accumulation mode, we distinguish natural and anthropogenically influenced aerosol composition by replacing a part of the sulfate mass M_{SU} by dust mass M_{DU} such that the fraction

$$f_{\text{SU}} = \frac{M_{\text{SU}}}{M_{\text{SU}} + M_{\text{DU}}} \quad (8)$$

takes values in between $f_{\text{SU}} = 0.6$ (natural) and $f_{\text{SU}} = 0.9$ (anthropogenic) and Eq. (7) corresponds to $f_{\text{SU}} = 1$.

Our investigations are based on 29 simulations with different aerosol conditions. These are constructed by linear interpolation between the clean–natural and the polluted–anthropogenic aerosol conditions with respect to mass concentration, number concentration, and chemical composition: Each aerosol condition is described by a vector $(f_{\text{SU}}, f_{\text{N}}, f_{\text{M}})$. The chemical dimension is described by f_{SU} and varied between the natural and anthropogenic composition, $0.6 \leq f_{\text{SU}} < 0.9$. The weighting of clean $C = (N_c, M_c)$ and polluted $P = (N_p, M_p)$ mass and number concentrations at fixed composition is described by $f = (f_{\text{N}}, f_{\text{M}})$ according to $(N, M) = fP + (1 - f)C$, where f_{M} and f_{N} vary between 0 and 1.

Figure 2 illustrates the resulting three-dimensional parameter space. The choice of the parameter space is, on the one hand, motivated by capturing the variability in the two prognostic moments of the aerosol distribution. By varying the composition in terms of SU and DU, we, on the other hand, try to change the effective ratio of CCN and INPs and thus the relative importance of the ice- and warm-phase pathways to precipitation formation. Table 2 provides a key to some specific aerosol conditions.

3. Results

Figure 3 shows the warm- and mixed-phase cloud that form by orographic lifting at the upwind slope of the mountain. Temperatures T in the warm cloud are everywhere above the freezing level (Fig. 3a), while

temperatures in the mixed-phase cloud take values in between the subfreezing surface temperature and the onset temperature of homogeneous freezing (Fig. 3b). The microphysical cloud processes are shown in detail in Figs. 4a and 5a).

The clouds form by activation (act) of aerosol particles to cloud droplets at the windward rim, especially in the lower half with stronger updrafts. Note that activation regions with apparently vanishing cloud mixing ratio occur because microphysical rates are diagnosed before and cloud variables after tracer transport in the time step. In-cloud activation creates additional droplets at a horizontal distance of ≈ 350 km from the domain boundary where the mountain slope is steepest and causes high supersaturations.

Some of the droplets activated above a height of 2 km in the mixed-phase cloud are converted into ice crystals by immersion freezing (freez). In contrast to cloud

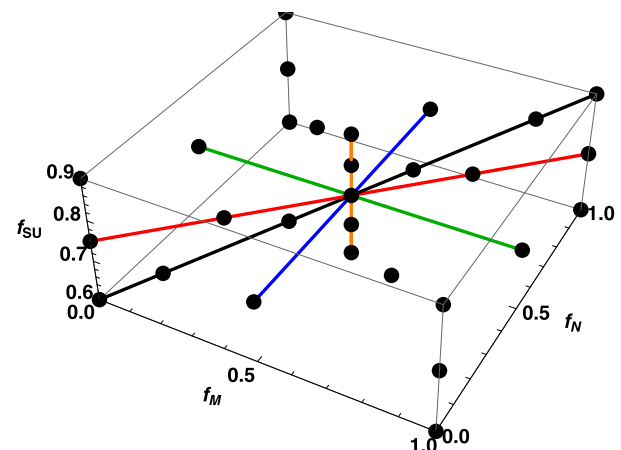


FIG. 2. Aerosol perturbations applied to probe susceptibilities are varied in a three-dimensional parameter space that is spanned by variations in composition, number, and mass as described by f_{SU} , f_{N} , and f_{M} , respectively (see text for details). Variations along the red axis correspond to increasingly polluted aerosol at constant composition. Along the orange axis, composition changes from natural to anthropogenic composition by replacing insoluble dust with soluble SO_4 . The black line combines mass, number, and sulfate increases. The blue line indicates more but smaller particles and the green line larger particles at fixed number.

TABLE 2. Key to 7 representative aerosol conditions out of the 29 total conditions considered and shown in Fig. 2. The conditions clean–natural and polluted–anthropogenic are extreme cases specified in Table 1. The other cases are interpolations between these two as specified by the interpolation parameters f_{SU} , f_N , and f_M (see text for details). As an example, the clean case features the same aerosol mass and number as the clean–natural case ($f_N = f_M = 0$), but its chemical compositions contains more sulfate than the “natural” case ($f_{\text{SU}} = 0.75$).

Name	f_{SU}	f_N	f_M	Description
Clean–natural	0.6	0	0	Specified in Table 1
Clean	0.75	0	0	Same aerosol mass and number as clean–natural, but of less natural composition
N poll	0.75	1	0	Same composition and aerosol mass as clean, but polluted aerosol number
Base	0.75	0.5	0.5	Same aerosol composition as clean, but with intermediate values of mass and number
M poll	0.75	0	1	Same composition and aerosol number as clean, but polluted aerosol mass
Polluted	0.75	1	1	Same aerosol mass and number as polluted–anthropogenic, but of less anthropogenic composition
Polluted–anthropogenic	0.9	1	1	Specified in Table 1

droplets, ice crystals have a nonnegligible sedimentation velocity. Sedimenting ice crystals form the lower-left part of the cloud in Fig. 5a that occurs downwind of activation and freezing. Sedimentation does not proceed vertically but at an angle because of the horizontal flow, as can also be observed for hydrometeors sedimenting downwind of the mountain (cf. Fig. 3).

Droplets and crystals grow by cond and vapor deposition on ice-phase hydrometeors (diff), respectively. Both processes together deplete the water vapor mixing ratio M_v , and their combined rate will be denoted as M_v sink (Figs. 4a and 5a). Coagulation (coag) converts small hydrometeors (i.e., cloud droplets and ice crystals) into large hydrometeors (i.e., raindrops, snowflakes, and graupel particles). Rain formation in the warm cloud proceeds via accretion (acc) and autoconversion (aut). The former is shifted downwind as compared to the latter (Fig. 4a) because accretion requires raindrops, which are initially produced by autoconversion. The glaciation of the mixed-phase cloud proceeds via the WBF process (Fig. 5a) and riming. WBF regions correspond to regions where M_v sink < diff.

The liquid saturation adjustment applied in the model ensures saturation ratios corresponding to water saturation, $S = 1$, in the warm cloud (not shown). This condition is also fulfilled in the major part of the mixed-phase cloud as shown in Fig. 5b. Only the outermost rim of the downwind side of the cloud at 380–400 km is completely glaciated.

To summarize, the mixing ratio of cloud water in the droplet category of the microphysics scheme M_{cl} is gradually transferred into the rain category M_{prl} in the warm cloud while the flow passes the mountain. The degree of this conversion can be characterized by the precipitation fraction

$$R_{\text{pr}} = \frac{M_{\text{prl}}}{M_{\text{prl}} + M_{\text{cl}}}, \quad (9)$$

which is illustrated in Fig. 4b (shaded regions). For the mixed-phase cloud, cloud water M_{cl} is converted into ice M_{ci} , rain M_{prl} , snow M_{prs} , and graupel M_{prg} . This conversion is described by the glaciation fraction

$$R_{\text{glac}} = \frac{M_{\text{ci}} + M_{\text{prs}} + M_{\text{prg}}}{M_{\text{cl}} + M_{\text{ci}} + M_{\text{pr}}}, \quad (10)$$

with $M_{\text{pr}} = M_{\text{prl}} + M_{\text{prs}} + M_{\text{prg}}$ denoting the sum of the mixing ratios of the large hydrometeor categories. The glaciation fraction is depicted in Fig. 5b (shaded regions).

The extent of the rain-dominated region defined by $R_{\text{pr}} > 0.5$ (cf. Fig. 4b) and of mixed-phase regions with $0.1 < R_{\text{glac}} < 0.9$ (cf. Fig. 5b) change with the aerosol background: Precipitation formation is delayed and glaciation sets in earlier for polluted conditions, as is expected from increased abundance of CCN and INPs. For the mixed-phase case, the location and extent of the cloud vary with the aerosol condition, while a corresponding effect is absent for the warm cloud (cf. red and blue contours in Figs. 4b and 5b). Changes in the extent of the mixed-phase cloud are caused by corresponding changes in the flow field (not shown). We find that the variability in the cloud extent and flow field is well correlated with the abundance of dust aerosol ($r^2 \approx 0.8$ in a bilinear fit of cloud extent as a function of total dust mass concentration and the number concentration of dust containing particles; not shown). As dust is a proxy for the abundance of INPs in different aerosol conditions, this correlation supports the concept that the changes in the flow field can be attributed to increased latent heat

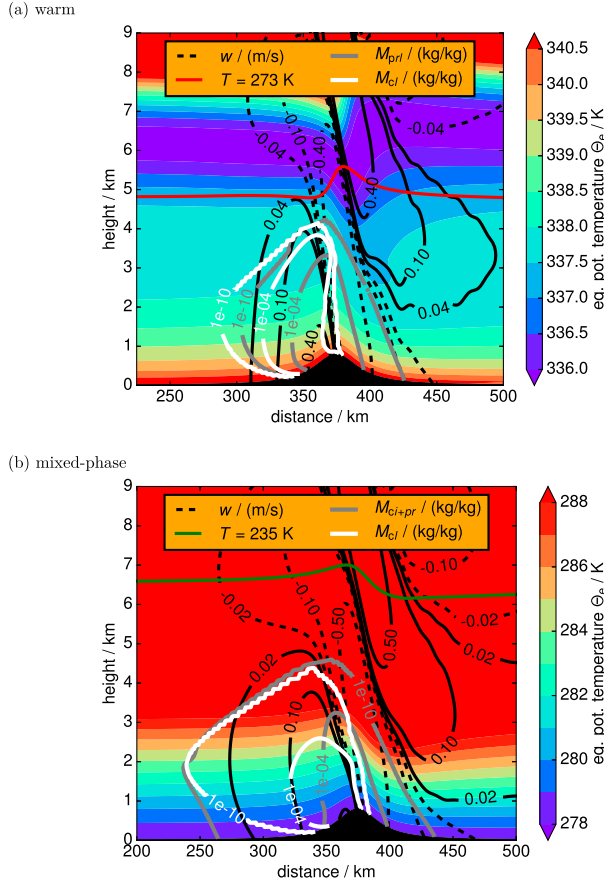


FIG. 3. Overview of (a) warm and (b) mixed-phase cloud. Color-filled contours show the steady-state profile of equivalent potential temperature θ_e , and black solid (positive) and dashed (negative) contour lines illustrate the steady-state updraft velocity field w that develops with the initial and boundary profile from Fig. 1. The orographic clouds are indicated by the mixing ratios of cloud water in the droplet category of the microphysics scheme M_{cl} (white contours) and water in hydrometeors categories with significant sedimentation velocity (gray contours), i.e., rain M_{pr} in the warm case and the sum of ice, rain, snow, and graupel M_{cl+pr} in the mixed-phase case. For the warm cloud, the freezing level (0°C) is indicated in red, while for the mixed-phase cloud, the onset level of homogeneous freezing (-38°C) is depicted in green. Note that a cirrus cloud forming behind the hill in the mixed-phase case is not shown.

release for more glaciated conditions and are not the result of nonsystematic variability in the quasi-steady state. We thus find a thermodynamic effect of INPs on the orographic mountain flow. This change on the flow does not affect our analysis.

a. Trajectory averages

Performing a susceptibility analysis on high-resolution simulation output bears two problems. First, if a variable is more strongly influenced by advection than by microphysics, susceptibilities would be artificially small because the former is largely independent of the details

of microphysics. Second, temporal delays (e.g., between the influence of aerosol on activation and precipitation formation) are not taken into account. Both issues are alleviated by choosing a Lagrangian framework for the analysis. Besides the use of cloud parcel models (Sorooshian et al. 2009; Feingold et al. 2013), the use of vertical averages or vertically integrated quantities like LWP (Jiang et al. 2010; Sorooshian et al. 2010; Duong et al. 2011; Terai et al. 2012; Jung et al. 2016; Dadashazar et al. 2017) roughly corresponds to averaging over the adiabatic trajectories of rising parcels in vertically developing clouds. For the horizontal development of orographic clouds, vertical averages would not approximate averages along parcel trajectories. Trajectories of orographic cloud parcels approximately follow lines of constant equivalent potential temperature θ_e . Averaging along the moist isentropes of parcel ascent can thus be replaced by averaging over the moist isentropes of mountain flow. The parcel approach cannot account for vertical mixing and the sedimentation of precipitation hydrometeors. Our analysis assumes that both effects can be neglected in comparison to the transport along the trajectories. Vertical mixing is expected to be small because of the quasi-stable stratification of our setup. The dominance of horizontal as compared to vertical transport of precipitation hydrometeors is illustrated by the flat slopes of falling precipitation in Fig. 3.

Our analysis is based on normalized sums of cloud properties $X^a(\theta_e, l)$,

$$\langle X^a \rangle(\theta_e) = \frac{1}{L(\theta_e)} \sum_l X^a(\theta_e, l), \quad (11)$$

where l denotes the position along a trajectory and the superscript a indicates the different aerosol conditions. We normalize the trajectory sum with the aerosol-independent length $L(\theta_e)$ that counts the number of grid boxes that the θ_e trajectory of the reference cloud (obtained as average over all aerosol conditions) runs within the cloud:

$$L(\theta_e) = \sum_l C(\theta_e, l), \quad \text{where} \\ C(\theta_e, l) = \begin{cases} 1 & \text{for } M_{cl+ci}^{\text{ref}} > 10^{-10} \text{ kg kg}^{-1} \\ 0 & \text{otherwise} \end{cases}. \quad (12)$$

We choose to normalize the trajectory sum to obtain meaningful values for the cloud properties. We use an aerosol-independent normalization, rather than calculating a conventional average, which amounts to normalizing with the aerosol-dependent number of cloudy grid points for a given aerosol condition, so that we do not mask the aerosol-dependent variability in trajectory

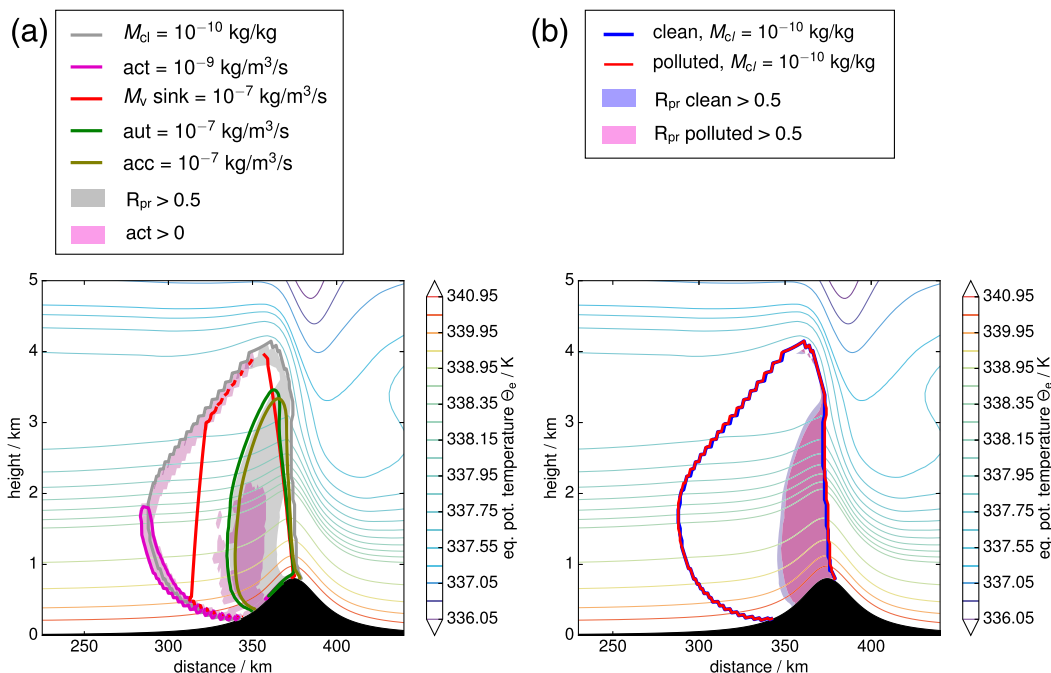


FIG. 4. Cloud microphysical process rates and aerosol effects on precipitation formation in the warm cloud. (a) Contour lines show rates of change in mass mixing ratios for the warm cloud as outlined by cloud water M_{cl} because of activation (act), net condensation (M_v sink), autoconversion (aut), and accretion (acc). Color-filled contours indicate regions with $act > 0$ and a rain fraction $R_{pr} = M_{pr}/(M_{pr} + M_{cl}) > 0.5$ [Eq. (9)]. Plots are based on averages over all aerosol conditions. (b) Cloud location as outlined by M_{cl} and $R_{pr} > 0.5$ (color-filled contours) for the clean and the polluted aerosol conditions (see Table 2).

lengths. As illustrated in Fig. 3, trajectories, or lines of constant θ_e , respectively, cross the mountain horizontally. The variables l and θ_e can thus be considered a horizontal and vertical coordinate, respectively, such that the normalized sum $\langle \cdot \rangle$ can be considered a horizontal average that results in profiles of cloud properties.

Figures 6–8 show such trajectory profiles of cloud characteristics for selected aerosol conditions obtained in this way. A comparison of the curves for the “base” and “M poll” cases, which lead to comparable cloud conditions, illustrates that aerosol mass and number perturbation have comparable effects on the profiles. Comparing the polluted–anthropogenic to polluted aerosol conditions shows that aerosol composition mainly matters for the glaciated part of the cloud, where it controls the amount of INP-active dust.

For the warm cloud, the average condensation rate, which corresponds to the sink of water vapor M_v in the absence of ice-phase diffusional growth, decreases as the height of the trajectories increases but is independent of the aerosol condition (Fig. 6b). As a result, the mixing ratios of cloud water M_{cl} and rainwater M_{pr} likewise decrease with height (Figs. 6c,d). As expected, droplet number N_{cl} increases with increasing pollution (Fig. 6e). The size of droplets as measured by their average mass

M_{cl}/N_{cl} decreases (Fig. 6f) although cloud water M_{cl} increases. For polluted aerosol conditions, M_{pr} is slightly decreased (Fig. 6c).

Despite the aerosol-induced differences in the flow pattern and extent of the mixed-phase cloud (Fig. 5b), the trajectory-averaged updraft $\langle W \rangle$ turns out to be independent of the aerosol condition, as is also the case in the warm cloud (Figs. 6a and 7a). Nevertheless, the vapor depletion rate, M_v sink, is slightly decreased for clean as compared to polluted conditions in the upper, glaciated part of the cloud (Fig. 7b). Here, an increase in aerosol means an increase in glaciation, which means an increase in diffusional vapor deposition and thus an increase in overall vapor depletion.

For the mixed-phase cloud, we distinguish cloud water from sedimenting hydrometeor classes, $M_{ci+pr} = M_{prl} + M_{prs} + M_{prg} + M_{ci}$, with the mixing ratios of ice crystals M_{ci} , rain M_{prl} , snow M_{prs} , and graupel M_{prg} . We may interpret M_{ci+pr} as precipitation: even if small ice crystals constitute cloud rather than precipitation, they rapidly grow by vapor deposition and coagulation with larger hydrometeors after sedimenting into the lower part of the cloud. In the lower part of the cloud, differences in M_{ci+pr} are dominated by rain with a compensation from graupel (Figs. 8d,e). The upper part is

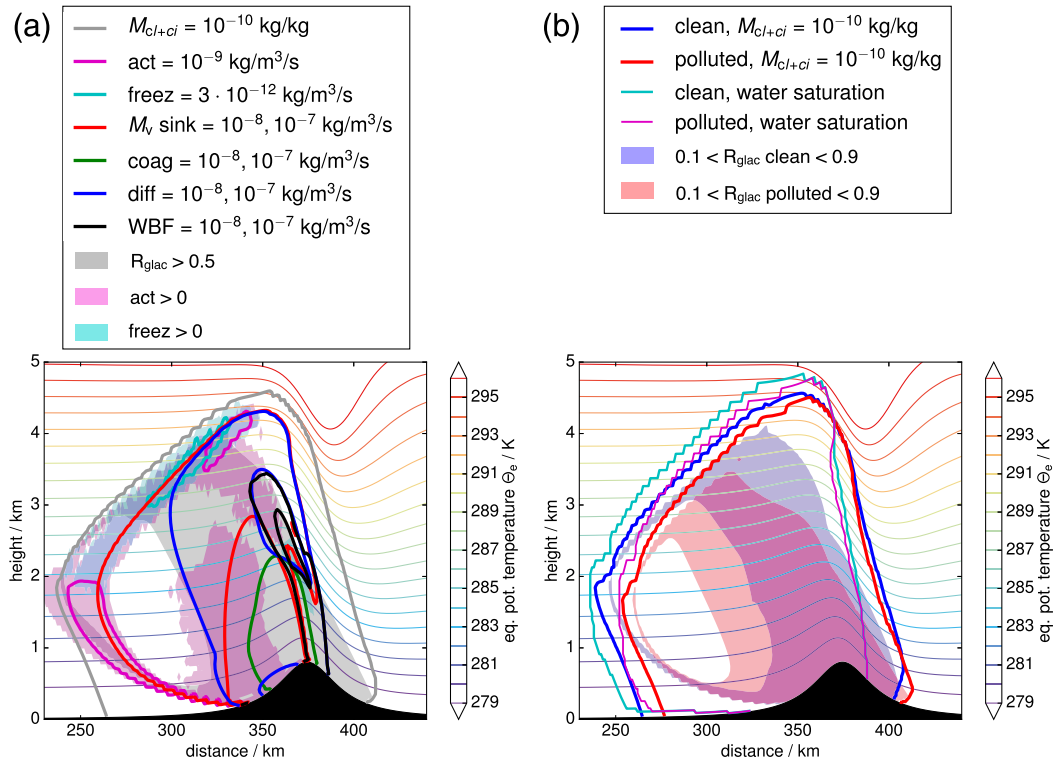


FIG. 5. Cloud microphysical process rates and aerosol effects on glaciation in the mixed-phase cloud. (a) Contour lines show rates of change in mass mixing ratios in the mixed-phase cloud as outlined by the sum of cloud water and ice M_{cl+ci} because of activation (act); freezing (freez); the total depletion of water vapor (M , sink), which includes net condensation and vapor deposition on ice-phase hydrometeors (diff); total coagulation (coag), including autoconversion, accretion, and riming; and the WBF process (WBF). Color-filled contours indicate regions with $act > 0$, $freez > 0$, and glaciation fractions $0.1 < R_{glac} = M_{ci+prg+prg}/M_{cl+ci+pr} < 0.9$. Plots are based on averages over all aerosol conditions. (b) Cloud location and extent as outlined by M_{cl+ci} and $0.1 < R_{glac} < 0.9$ (color-filled contours) for the clean and the polluted aerosol conditions (see Table 2) as well as outlines of water saturation.

dominated by M_{ci} (Fig. 8a). Snow qualitatively follows the behavior of M_{ci} but is quantitatively less relevant (Figs. 8a,f).

The lower part of the mixed-phase cloud depends on aerosol conditions in a way qualitatively similar to the warm cloud when considering M_{ci+pr} as precipitation mixing ratio (Figs. 6c and 7c). Quantitatively, the precipitation response is more pronounced in the mixed-phase case than in the warm case. As glaciation increases with increasing height and decreasing temperature, the signals in M_{cl} and M_{ci+pr} to increasing pollution change their sign: pollution increases the number concentration of INPs and leads to an increased ice crystal number concentration N_{ci} and mixing ratio M_{ci} (Figs. 8a,b). As cold microphysics increases in importance, cloud liquid is depleted (Fig. 7d).

The signal in droplet size remains decreasing for increasing pollution (Fig. 7f), while ice crystal size features three regimes (Fig. 8c): Crystal size decreases with increasing pollution in the lower and upper parts of the cloud. In between, a sudden increase in ice mixing ratio

with height and pollution, which coincides with the shifting location and extension of the mixed-phase region (Fig. 5), corresponds to increasing crystal sizes.

To summarize, the trajectory profiles show that the response of the precipitation mixing ratio to aerosol perturbations in the warm as well as in the mixed-phase orographic cloud is buffered as compared to the signals in cloud water and cloud ice.

b. Cloud water budgets

The buffered precipitation response described in the previous section can be understood as a consequence of balancing the budget of cloud water M_{cl} in the cloud (i.e., the need of sources and sinks of cloud water to compensate for all aerosol conditions). The main source of M_{cl} is cond. In mixed-phase clouds, the melting (melt) of small ice crystals provides an additional, smaller source. Possible sink processes are aut, acc, ice-droplet riming (ic-rim), snow-droplet riming (sc-rim), graupel-droplet riming (gc-rim), and evaporation (evp), which includes the WBF process, and the freezing of cloud

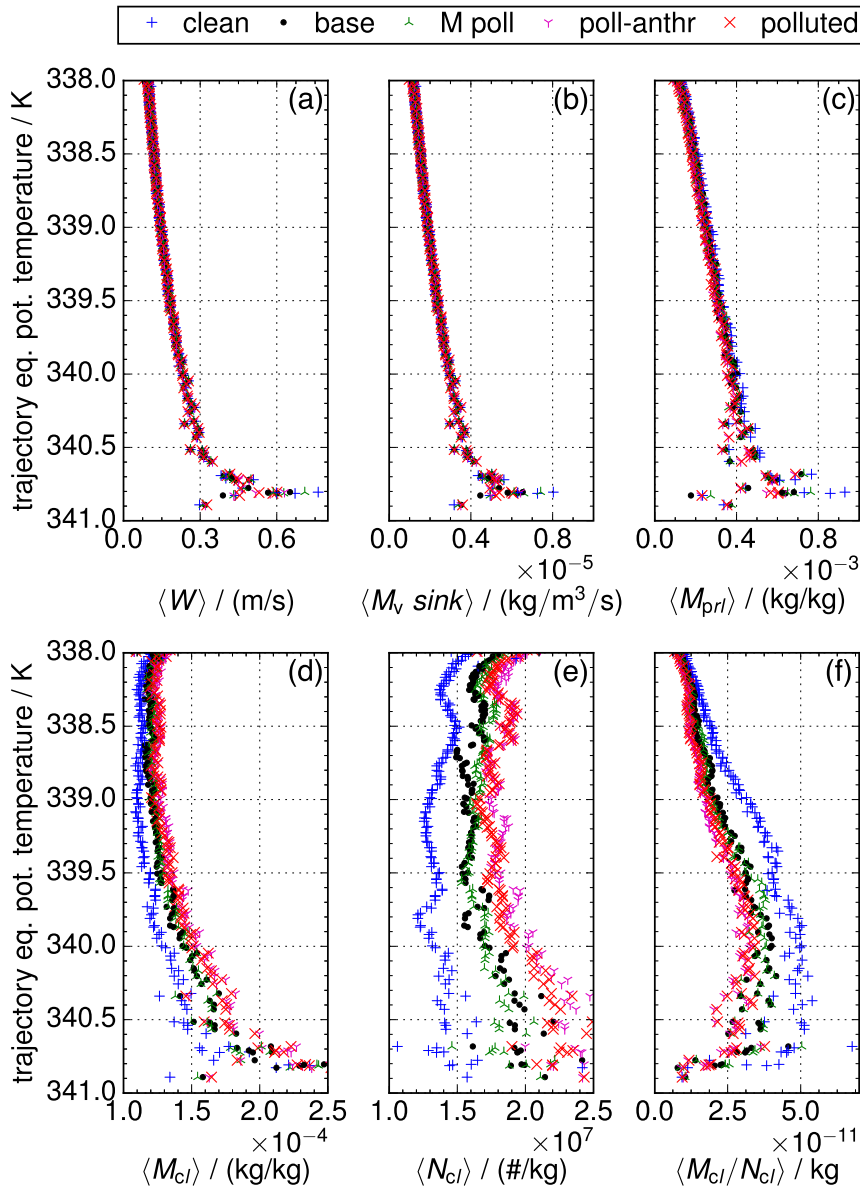


FIG. 6. Trajectory profiles of the warm cloud with equivalent potential temperature θ_e as the “height coordinate” on the y axis and trajectory averages on the x axis of (a) updraft W ; (b) vapor depletion rate M_v sink, which corresponds to the condensation rate; (c) rainwater mixing ratio $M_{pri} = M_{pr}$; (d) cloud water mixing ratio M_{cl} ; (e) droplet number mixing ratio N_{cl} ; and (f) average droplet mass M_{cl}/N_{cl} . Colors indicate specific aerosol conditions (Table 2).

droplets. As sedimentation is negligible for cloud droplets and entrainment of cloud water is not parameterized in the model used for this study, these processes

do not affect the cloud water budget. For normalized sums [Eq. (11)] along trajectories, we can thus study the following balanced cloud water budget B_{cl} :

$$\begin{aligned}
 0 &= \langle B_{cl} \rangle, \\
 &= \langle \text{cond} \rangle + \langle \text{melt} \rangle - \langle \text{evp} \rangle - \langle \text{aut} \rangle - \langle \text{acc} \rangle - \langle \text{ic-rim} \rangle - \langle \text{sc-rim} \rangle - \langle \text{gc-rim} \rangle - \langle \text{freez} \rangle \\
 &\approx \langle M_v \text{ sink} \rangle - \underbrace{(\langle i\text{-diff} \rangle + \langle s\text{-diff} \rangle + \langle g\text{-diff} \rangle + \langle \text{aut} \rangle + \langle \text{acc} \rangle + \langle \text{ic-rim} \rangle + \langle \text{sc-rim} \rangle + \langle \text{gc-rim} \rangle)}_{= \langle M_{cl+pr} \text{ prod} \rangle}, \tag{13}
 \end{aligned}$$

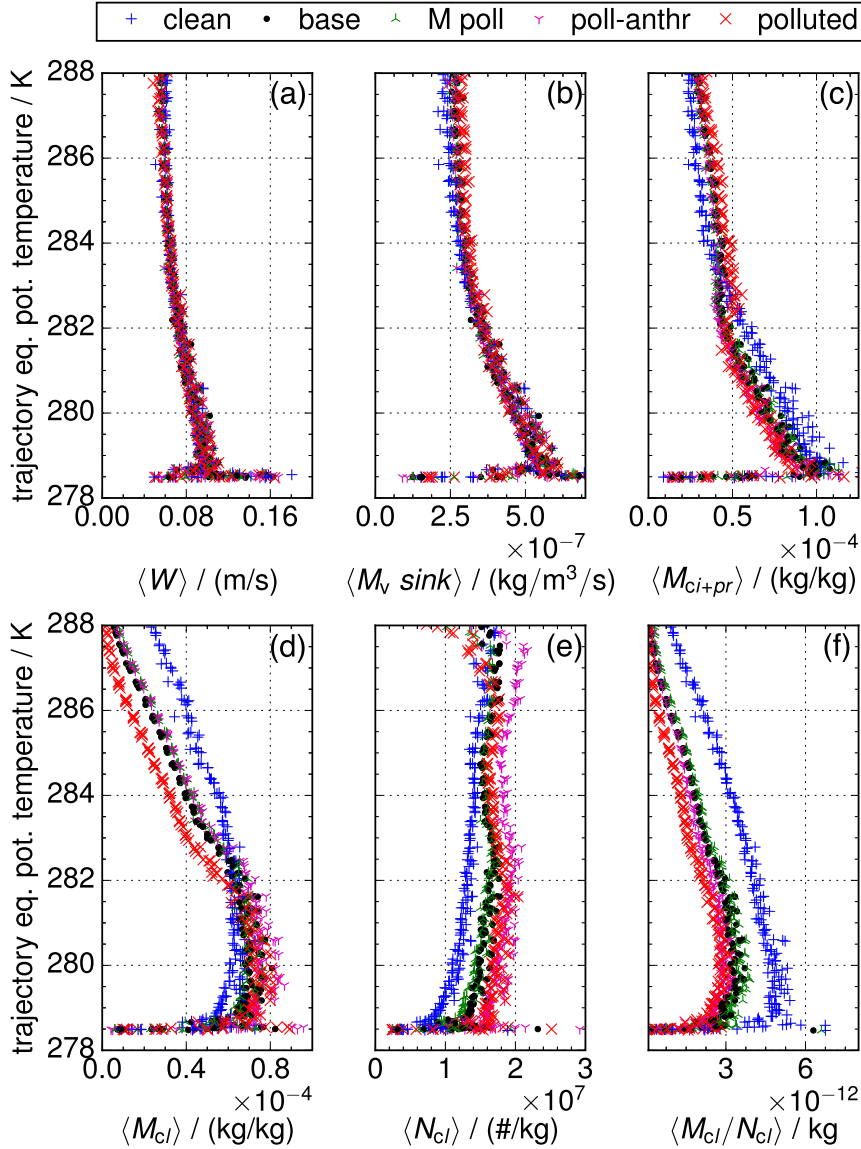


FIG. 7. As in Fig. 6, but for the mixed-phase cloud and with the precipitation mixing ratio M_{ci+pr} instead of rain.

where we have substituted $\langle \text{cond} \rangle = \langle M_v \text{ sink} \rangle - \langle i\text{-diff} \rangle - \langle s\text{-diff} \rangle - \langle g\text{-diff} \rangle$ and neglected freezing, melting, and evaporation to obtain the approximate expression in the third row of Eq. (13). Freezing can be neglected because the size of freezing cloud droplets is very small compared to the typical sizes that ice crystals quickly reach by vapor deposition. Melting and evaporation can be neglected in our case because our setup assumes subfreezing surface temperatures and because it features a complete conversion of cloud water. All the sink terms are sources of the precipitation mixing ratio M_{ci+pr} such that they constitute the total precipitation production (precip prod). This balance is approximately

met by our simulations (cf. graphs of M_v sink and precip prod in Figs. 9a and 10a).

As discussed in the context of Figs. 6 and 7, the source term $\langle M_v \text{ sink} \rangle$ in Eq. (13) is independent of the aerosol background for the warm cloud and in the lower part of the mixed-phase cloud. When comparing two simulations with different aerosol conditions, an aerosol-induced change to one of the sink processes in Eq. (13) thus has to be compensated by an opposite change in another sink process to ensure that their sum still matches the constant source term. In the upper part of the mixed-phase cloud, $\langle M_v \text{ sink} \rangle$ increases with increasing glaciation, and aerosol-induced changes in

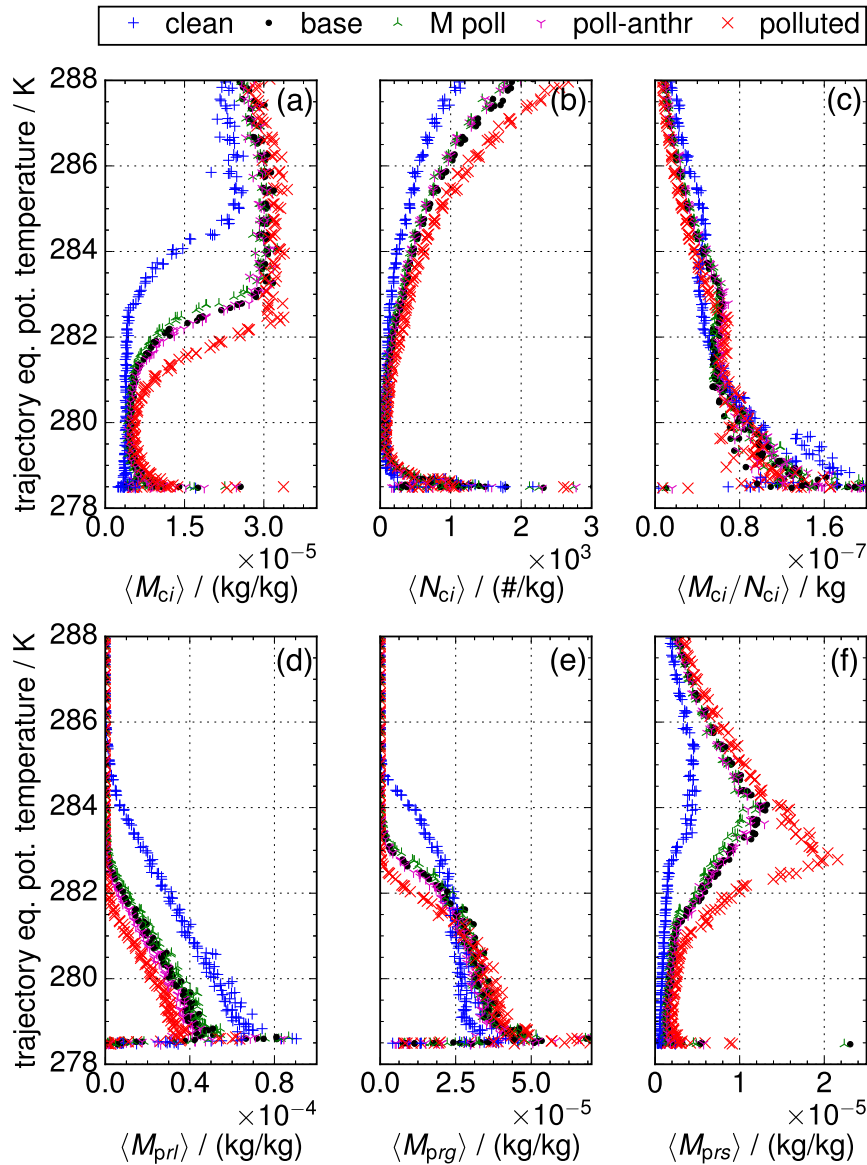


FIG. 8. As in Fig. 7, but for (a) ice water mixing ratio M_{ci} , (b) ice crystal number N_{ci} , (c) average ice crystal mass M_{ci}/N_{ci} , (d) rainwater mixing ratio M_{pri} , (e) graupel water mixing ratio M_{prg} , and (f) snow water mixing ratio M_{prs} .

precipitation formation pathways are constrained to be consistent with this increase.

The compensating behavior of the different processes contributing to precipitation production is illustrated in Figs. 9b and 10b: For the warm cloud, a decrease in autoconversion with increasing pollution is compensated by a matching increase in accretion (Fig. 9b). Comparing the vertical difference profiles of microphysical rates in the mixed-phase cloud illustrates that changes in autoconversion and cloud-droplet riming compensate each other (Fig. 10b). This shift is driven by an increased abundance of ice. Pollution-induced shifts

from graupel to snow lead to compensating changes in snow-droplet and graupel-droplet riming. Changes in accretion seem to correspond to a combination of changes in graupel-cloud riming and diffusional growth. In the upper part of the cloud, a partial compensation between changes in ice-droplet riming and diffusion may be identified. The compensating tendencies between microphysical rates are not restricted to the relationship between the two aerosol conditions compared in Figs. 9 and 10. For most trajectories, we find strong negative correlations (coefficient of determination $r^2 > 0.8$) between aerosol-induced changes in the rates of

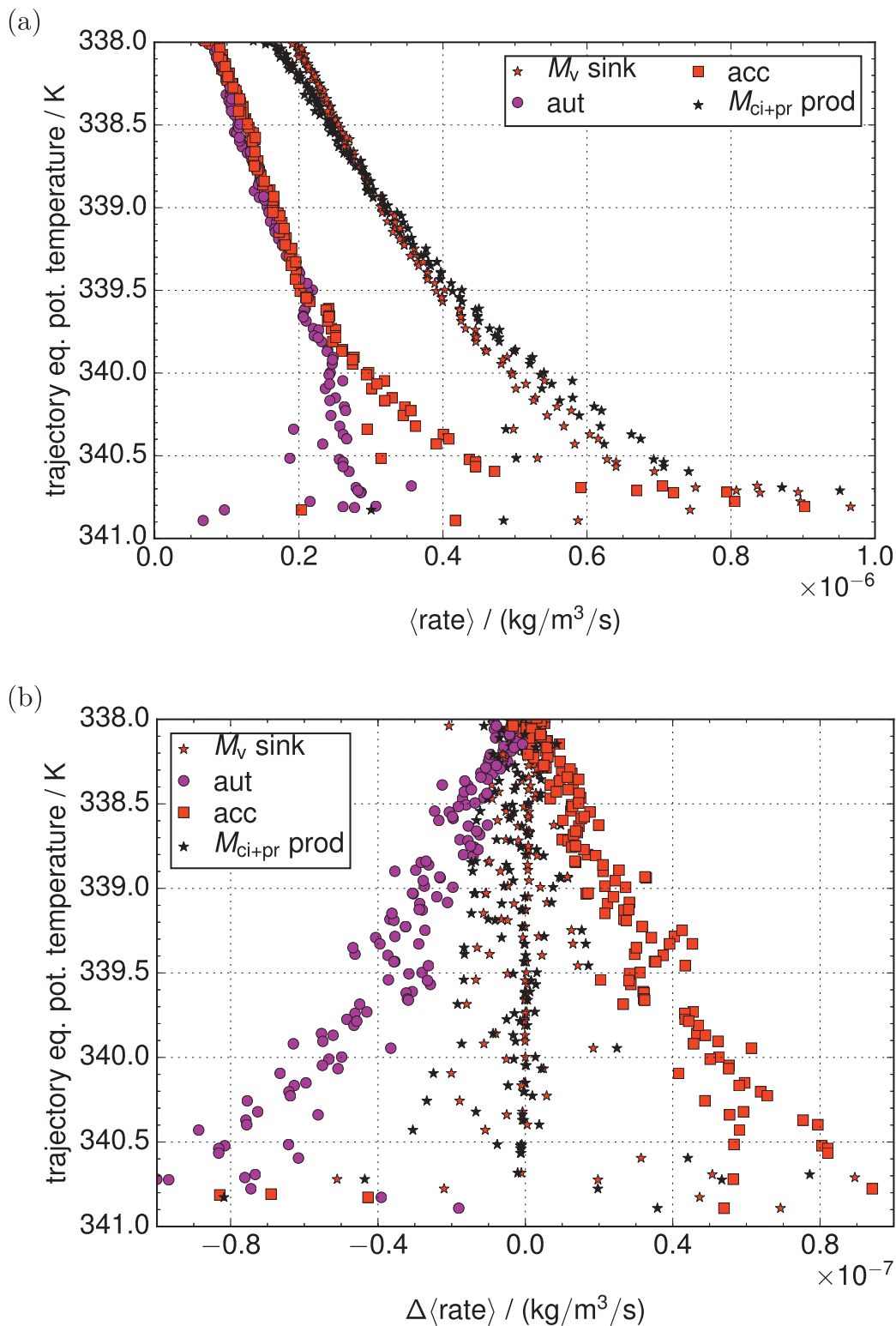


FIG. 9. The droplet water budget of the warm cloud consists of the vapor depletion rate (M_v sink) and the rates of autoconversion (aut) and accretion (acc), whose sum amounts to the total rain production $M_{ci+pr} = M_{pr}$ for trajectory profiles of (a) these rates for the "base" aerosol condition (Table 2) and (b) their differences between polluted (P) and clean (C) aerosol conditions ($P - C$).

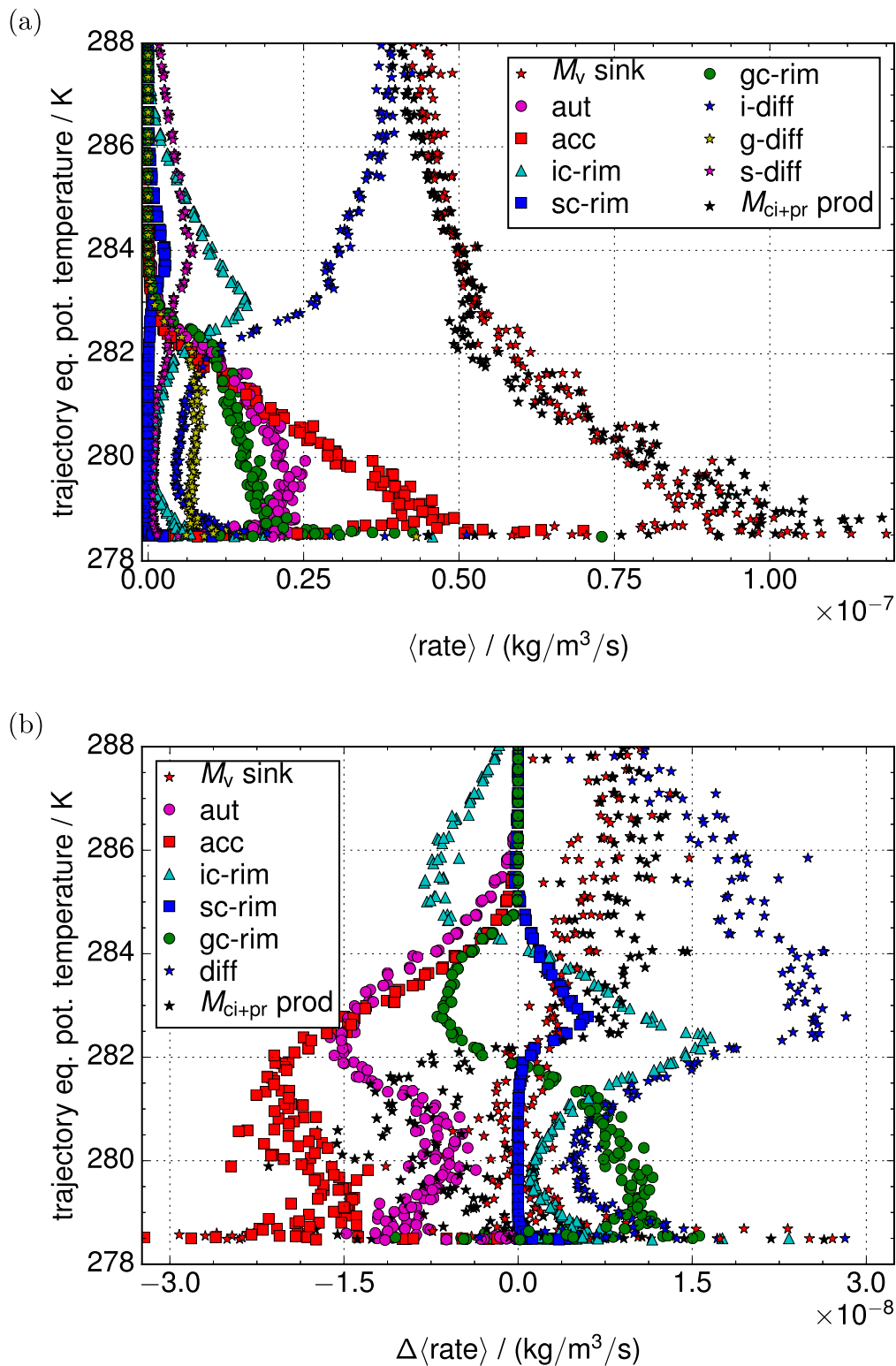


FIG. 10. As in Fig. 9, but for the mixed-phase cloud and with additional rates of ice–cloud riming (ic-rim), snow–cloud riming (sc-rim), graupel–cloud riming (gc-rim), diffusional growth of ice (*i*-diff), snow (*s*-diff) and graupel (*g*-diff) and the summed diffusional growth (diff).

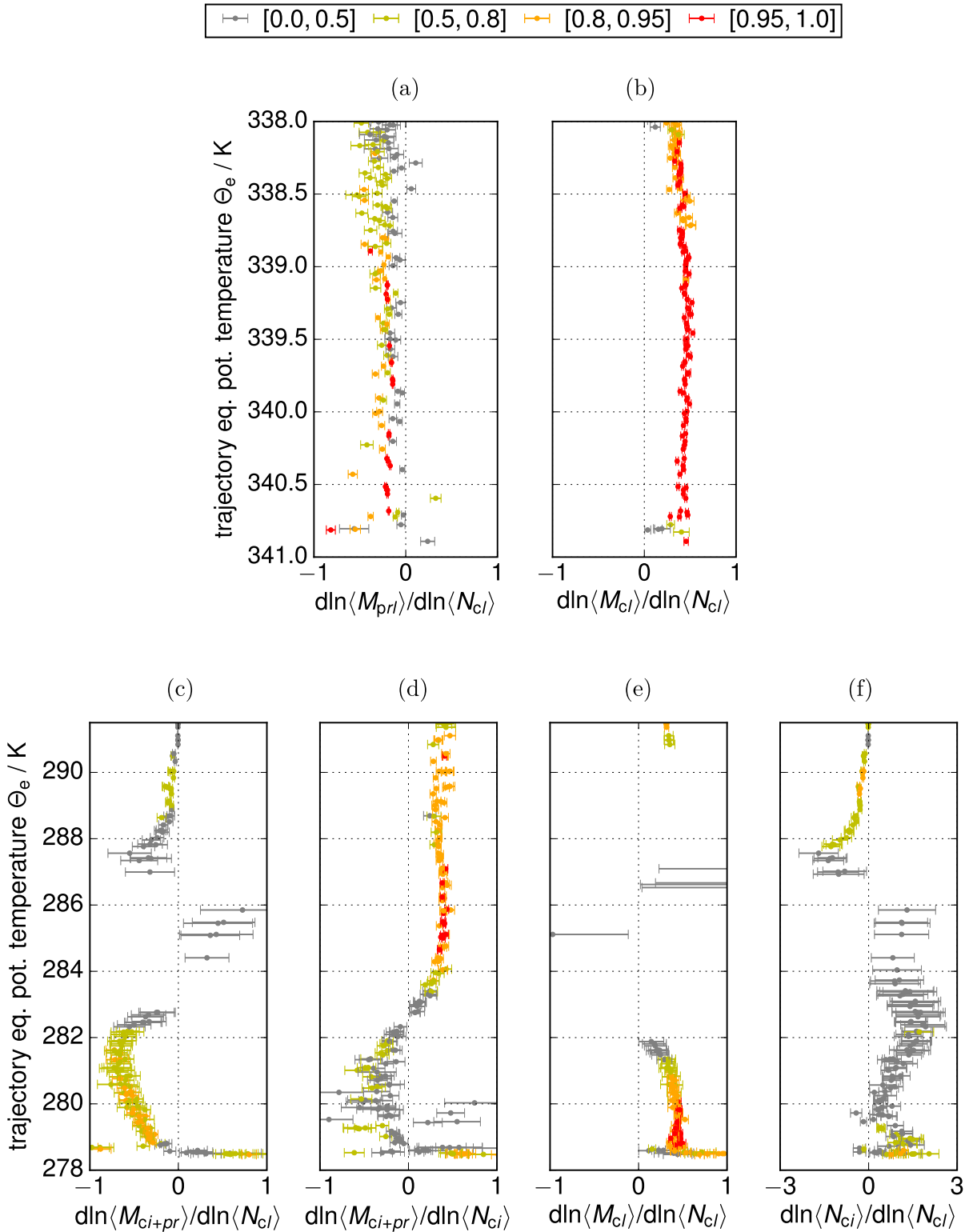


FIG. 11. Total precipitation susceptibilities of rainwater mixing ratio M_{prl} to (a) droplet number N_{cl} for the warm cloud and of the precipitation mixing ratio M_{ci+pr} to (c) droplet number N_{cl} and (d) crystal number N_{ci} . Also shown are (b),(e) the cloud liquid adjustment to droplet number, $d\ln M_{cl}/d\ln N_{cl}$ in the (b) warm- and (e) mixed-phase cloud, and (f) the ice crystal number adjustment to droplet number $d\ln N_{ci}/d\ln N_{cl}$ in the mixed-phase cloud. Data points represent fit coefficients according to Eq. (14) as a function of equivalent potential temperature θ_e . The color scale encodes the value of the coefficient of determination r^2 of the corresponding regression. Error bars show the 95% confidence interval of the fitted coefficients/susceptibilities. Only fits significant at the 95% level based on a two-sided t test have been considered.

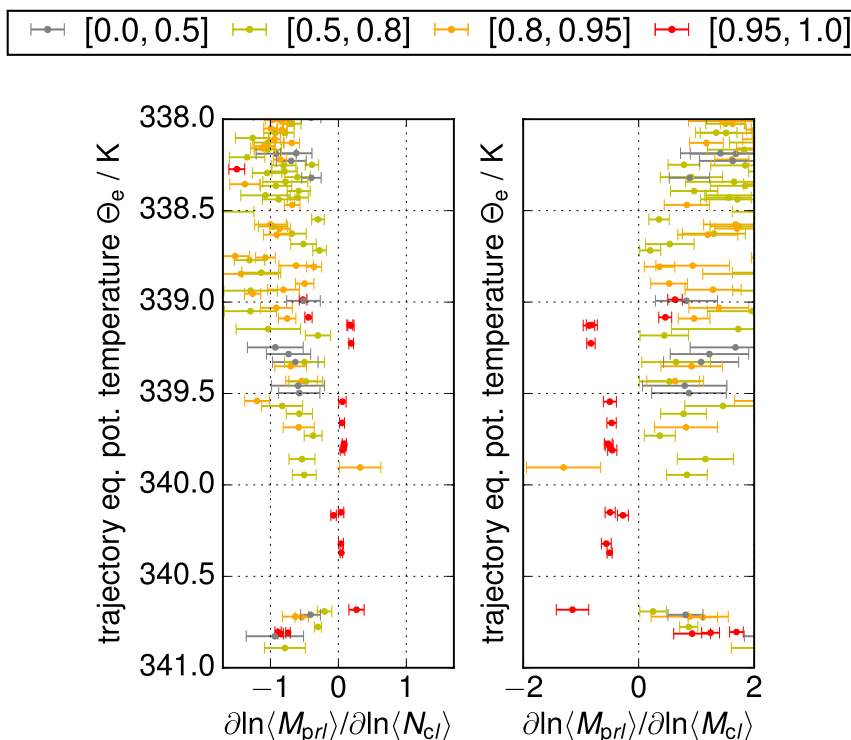


FIG. 12. Partial precipitation susceptibilities of warm rainwater M_{prl} to droplet number N_{cl} and cloud droplet liquid M_{cl} as fitted according to Eq. (15) as a function of equivalent potential temperature θ_e . The color scale encodes the value of the coefficient of determination r^2 of the bilinear regression. Error bars show the 95% confidence interval of the fitted coefficients/susceptibilities. Only fits with an overall significance (F test) and significant coefficients (two-sided t test) at the 95% level have been considered.

autoconversion and accretion in the warm cloud and the sum of autoconversion and accretion and riming in the mixed-phase cloud (not shown).

In summary, the constraint of retaining a balanced budget of cloud water M_{cl} means that different precipitation production processes need to adapt in compensating ways to an aerosol perturbation. While an aerosol perturbation can thus redistribute the pathways of precipitation formation, the total precipitation production in nonglaciaded cloud parts remains largely constant and is thus almost completely buffered. The only control aerosols have on precipitation production is via variability in INPs that change the glaciation state and thus control the depletion of water vapor by deposition on ice-phase hydrometeors.

c. Precipitation susceptibility

The aerosol dependence of the precipitation mixing ratio M_{ci+pr} in the upper glaciated part of the mixed-phase cloud from Fig. 7 can be explained by the glaciation-mediated aerosol dependence of the sink of M_v . For the lower part of the mixed-phase cloud and the

warm cloud, however, M_{ci+pr} changes with the aerosol condition although the sink of M_v is aerosol independent. Here, the redistribution of precipitation formation pathways corresponds to a redistribution of the total hydrometeor mixing ratio $M_{cl+ci+pr}$ between the different categories. The precipitation mixing ratio thus changes although its source rate does not. This is a situation typically observed in fully equilibrated systems. Shortly after a perturbation, in contrast, the source rate and mixing ratio would be correlated [recall the discussion of Eqs. (2) and (3)]. To quantify the redistribution effects and discuss their relationship to the budget constraint, we apply the concept of precipitation susceptibility [Eq. (1)].

We determine total precipitation susceptibilities $d\ln M_{ci+pr}/d\ln N_c$ to cloud droplet and/or ice crystal number concentration, $N_c = N_{cl}, N_{ci}$, individually for each trajectory, labeled by its value of θ_e . The dependence of the susceptibility on the trajectory corresponds to regime dependence because the height of a trajectory determines its temperature and condensation rate. Different trajectories show a strong meteorological covariability between cloud variables. This

variability is stronger than the variability from different aerosol conditions and would mask the aerosol effect when disregarding the trajectory dependence of susceptibilities. Based on the variability arising for the 29 different aerosol conditions simulated, we thus fit for each trajectory the log-linear model

$$\ln\langle M_{\text{ci+pr}} \rangle(\theta_e) = s_{N_c} \ln\langle N_c \rangle(\theta_e) + c(\theta_e), \quad (14)$$

where c is the axis intercept of the fit and coefficients s_{N_c} correspond to total susceptibilities. The validity of this linear model is quantified by the correlation coefficient r or the coefficient of determination r^2 .

Total precipitation susceptibilities to droplet number are negative for the warm as well as for the lower part of the mixed-phase cloud (Figs. 11a,c), as is expected for a classical lifetime effect {recall that our definition of precipitation susceptibility [Eq. (1)] omits the conventional minus sign}. The mixed-phase susceptibility to droplet number with a value of about -0.5 is stronger than the warm value of about -0.25 . The precipitation mixing ratio in the upper part of the mixed-phase cloud, which is dominated by ice crystals, is not correlated to cloud droplet number (Fig. 11c). Instead, it is well predicted by the number of ice crystals, which is in turn not correlated to $M_{\text{ci+pr}}$ in the lower part (Fig. 11d).

Total precipitation susceptibilities comprise the effects of aerosol-induced changes in cloud droplet and ice crystal number and adjustments to these changes. For the warm cloud, a decomposition into number effect and adjustments reveals how the budget constraint controls the partitioning of cloud and rainwater and thus precipitation susceptibility: Eq. (1) corresponds to a bilinear regression

$$\ln\langle M_{\text{prl}} \rangle(\theta_e) = s_{N_{\text{cl}}} \ln\langle N_{\text{cl}} \rangle(\theta_e) + s_{M_{\text{cl}}} \ln\langle M_{\text{cl}} \rangle(\theta_e) + c(\theta_e), \quad (15)$$

with coefficients $s_{N_{\text{cl}}} = \partial \ln\langle M_{\text{prl}} \rangle / \partial \ln\langle N_{\text{cl}} \rangle$ and $s_{M_{\text{cl}}} = \partial \ln\langle M_{\text{prl}} \rangle / \partial \ln\langle M_{\text{cl}} \rangle$ corresponding to partial susceptibilities. Fitted results for partial susceptibilities are shown in Fig. 12. The partial precipitation susceptibility with respect to cloud droplet number $s_{N_{\text{cl}}}$ tends to be positive when only considering data points with $r^2 > 0.95$. This

result seems counterintuitive and in contrast to the classical lifetime effect. It arises from higher-order adjustments in the cloud to reequilibrate the budget: An increase in cloud droplet number reduces autoconversion and thus requires an increase in accretion to keep precipitation production constant. At fixed M_{cl} , accretion can only be increased by increasing M_{prl} . Along similar lines, the budget constraint explains a negative partial susceptibility $s_{M_{\text{cl}}}$: At fixed N_{cl} , an increase in M_{cl} increases autoconversion and accretion, which is then compensated by a decrease in accretion mediated by a decrease in M_{prl} . In other words, the negative values of $s_{M_{\text{cl}}}$ describe a redistribution of rainwater, which decreases, to cloud water, which increases, and corresponds to a decreasing precipitation fraction.

The budget constraint can be formalized by expressing partial susceptibilities as an implicit derivative of the balance equation [Eq. (13)]:

$$\begin{aligned} \frac{\partial \ln M}{\partial \ln N} &= - \frac{\frac{\partial B_{\text{cl}}[N, M(N)]}{\partial \ln N}}{\frac{\partial B_{\text{cl}}[N, M(N)]}{\partial \ln M}} = - \frac{\frac{\partial \sum r[N, M(N)]}{\partial \ln N}}{\frac{\partial \sum r[N, M(N)]}{\partial \ln M}} \\ &= - \frac{\sum \frac{\partial \ln r[N, M(N)]}{\partial \ln N} r[N, M(N)]}{\sum \frac{\partial \ln r[N, M(N)]}{\partial \ln M} r[N, M(N)]}, \quad (16) \end{aligned}$$

where we have omitted indices and average brackets for brevity and sums run over $r \in \{-M_v \text{ sink, aut, acc, ic-rim, is-rim, ig-rim, } i\text{-diff, } s\text{-diff, } g\text{-diff}\}$. The rearrangement on the right-hand side shows the relationship between susceptibilities of conversion rates r and state variables M and N . Assuming that rate susceptibilities take values of magnitude 1, the rearrangement also illustrates that conversion processes with absolutely small rates like evaporation, melting, and freezing in our case can be neglected when estimating the sign of a partial susceptibility.

From Eq. (16), the sign of the partial precipitation susceptibility to droplet number in the warm cloud follows to be positive,

$$\text{sgn} \left(\frac{\partial \ln M_{\text{prl}}}{\partial \ln N_{\text{cl}}} \right) = \text{sgn} \left[\frac{\partial (\text{aut} + \text{acc} - M_v \text{ sink}) / \partial \ln N_{\text{cl}}}{\partial (\text{aut} + \text{acc} - M_v \text{ sink}) / \partial \ln M_{\text{prl}}} \right] = \frac{(-1) + (0) - (0)}{(0) + (+1) - (0)} = +1, \quad (17)$$

where the evaluation is based on assuming that (i) autoconversion decreases with increasing N_{cl} and is independent of M_{prl} , (ii) accretion increases with increasing M_{prl} and is independent of N_{cl} , and (iii) condensation

(which is identical to $M_v \text{ sink}$ for the warm cloud) is independent of both variables and all rates are trajectory-averaged rates as functions of trajectory-averaged cloud variables. Assuming that autoconversion and accretion

both increase with increasing M_{cl} results in $s_{M_{cl}} < 0$, as observed. It needs to be stressed that trajectory-averaged rates as functions of trajectory-averaged variables do not follow the functional forms implemented in the cloud microphysics scheme. This difference explains that fitted values of partial susceptibilities differ from the values derived based on the microphysical equations in [Glassmeier and Lohmann \(2016\)](#). This is also the reason that we do not include the rain dependence of SB auto-conversion ([Glassmeier and Lohmann 2016](#)) in assumption (i). Based on Eq. (1) in combination with the signs of the partial susceptibilities (Fig. 12a) and a positive adjustment $d\ln M_{cl}/d\ln N_{cl}$ (Fig. 11b), we conclude that the negative value of the total precipitation susceptibility to droplet number is the result of the negative adjustment term overcompensating the positive partial susceptibility. This is not surprising for a fully equilibrated system.

By considering all sedimenting hydrometeors as precipitation, the equivalent of Eq. (1) for adjustments in the lower part of the mixed-phase cloud reads

$$\begin{aligned} \frac{d\ln M_{ci+pr}}{d\ln N_{cl}} &= \frac{\partial \ln M_{ci+pr}}{\partial \ln N_{cl}} + \frac{\partial \ln M_{ci+pr}}{\partial \ln M_{cl}} \frac{d\ln M_{cl}}{d\ln N_{cl}} \\ &+ \frac{\partial \ln M_{ci+pr}}{\partial \ln N_{ci}} \frac{d\ln N_{ci}}{d\ln N_{cl}}. \end{aligned} \quad (18)$$

Given our limited dataset of 29 aerosol conditions and cross correlations between the variables, we refrain from performing the three-dimensional regression corresponding to Eq. (15). Instead, we limit our analysis to an analytical estimation of partial susceptibilities similar to Eq. (17):

$$\begin{aligned} \text{sgn} \left(\frac{\partial \ln M_{ci+pr}}{\partial \ln N_{cl}} \right) &= \text{sgn} \left[- \frac{\partial \text{aut} / \partial \ln N_{cl}}{\partial (\text{acc} + \text{rim} + \text{diff}) / \partial \ln M_{ci+pr}} \right] \\ &= +1, \end{aligned} \quad (19)$$

$$\begin{aligned} \text{sgn} \left(\frac{\partial \ln M_{ci+pr}}{\partial \ln M_{cl}} \right) &= \text{sgn} \left[- \frac{\partial (\text{aut} + \text{acc} + \text{rim}) / \partial \ln M_{cl}}{\partial (\text{acc} + \text{rim} + \text{diff}) / \partial \ln M_{ci+pr}} \right] \\ &= -1, \end{aligned} \quad (20)$$

$$\begin{aligned} \text{sgn} \left(\frac{\partial \ln M_{ci+pr}}{\partial \ln N_{ci}} \right) &= \text{sgn} \left[- \frac{\partial (\text{rim} + \text{diff}) / \partial \ln N_{ci}}{\partial (\text{acc} + \text{rim} + \text{diff}) / \partial \ln M_{ci+pr}} \right] \\ &= -1, \end{aligned} \quad (21)$$

where we have assumed that all partial derivatives with the exception of $\partial \text{aut} / \partial \ln N_{cl}$ are positive and omitted nonsusceptible rates. The signs of $s_{N_{cl}}$ and $s_{M_{cl}}$ are the same as in the warm case and can be interpreted in the same way. As the ice-phase variables in the mixed-phase

cloud feature strong covariability, N_{ci} can be interpreted as a proxy for the importance of ice- and mixed-phase pathways. The positive partial susceptibility $s_{N_{ci}} = \partial \ln M_{ci+pr} / \partial \ln N_{ci}$ means that at fixed N_{cl} and fixed M_{cl} , a shift from warm to cold pathways requires a reduction in M_{ci+pr} to reequilibrate the budget. Such a reduction is needed because ice-phase hydrometeors contribute to precipitation production not only by coalescence like rain but also by diffusion. Consequently, ice-phase hydrometeors produce precipitation more efficiently such that only a smaller amount of frozen hydrometeors as compared to rain is needed to cause the same total precipitation production rate. With positive adjustments $d\ln M_{cl}/d\ln N_{cl}$ and $d\ln N_{ci}/d\ln N_{cl}$ (Figs. 11e,f), the sign of mixed-phase precipitation susceptibility to droplet number is dominated by adjustments in the same way as warm precipitation susceptibility. The liquid and ice adjustments enhance each other because both terms in Eq. (18) are positive.

4. Conclusions

In an idealized, two-dimensional modeling study, we have explored the sensitivity of warm- and mixed-phase orographic precipitation to aerosol backgrounds that simultaneously vary in their abundance of cloud condensation nuclei (CCN) and ice nucleating particles (INPs). For quantification, we adapt the concept of precipitation susceptibility [Eq. (1)] to orographic clouds. To account for the horizontal rather than vertical development of orographic clouds, our analysis is based on averages of variables along moist isentropes [Eq. (11)], which trace parcel trajectories, rather than vertical averages. For warm, mixed-phase, and glaciated trajectories, we generally find low precipitation susceptibilities, which means that the precipitation response to aerosol perturbations is buffered as compared to the response of cloud variables like droplet number concentration and ice water path (Figs. 6–8).

The Lagrangian perspective of the trajectory approach allows us to formulate a budget equation for cloud water M_{cl} . Under steady-state conditions, this budget is balanced, which constrains the total precipitation formation to match the depletion of water vapor caused by the mountain flow [Eq. (13)]. In our simulations, the evaporation of cloud droplets is negligible such that vapor depletion corresponds to condensation in the warm cloud and to condensation and vapor deposition on ice-phase hydrometeors in the mixed-phase cloud. Condensation is independent of the aerosol background in our model because of the applied saturation adjustment. For the warm cloud, the application of a condensation scheme that allows

for supersaturations with respect to water could introduce an aerosol dependence of condensation if changes in (the location of) latent heat release changed the flow field or if supersaturation was sustained until a trajectory leaves the cloud. Both scenarios are probably not very important in our simulations. For the mixed-phase cloud, the saturation adjustment might limit the aerosol effect on vapor depletion: With saturation adjustment, WBF-active cloud regions feature water saturation, although a lower saturation ratio in between water and ice saturation is expected (Korolev 2007). Increased glaciation shifts saturation closer to ice saturation and thus increases diffusional vapor deposition. When applying a saturation adjustment, this effect is limited to shifting mixed-phase regions to full glaciation and does not allow for increased vapor deposition in mixed-phase regions.

The balance constraint on the precipitation production rate explains the buffered precipitation susceptibility. A change in the aerosol background leads to a redistribution among the different pathways of precipitation formation, but the total amount of precipitation formation can only increase because of increased glaciation and a shift from condensation to vapor deposition as discussed in the previous paragraph. In the warm cloud, aerosol-induced changes in autoconversion and accretion compensate each other, polluted conditions favoring accretion because autoconversion efficiency is reduced by smaller droplet sizes, which leads to an accumulation of cloud water. In the mixed-phase cloud, precipitation production via collision-coalescence is replaced by riming for more polluted aerosol conditions, which correspond to increased glaciation and vapor deposition. Under polluted conditions, glaciation proceeds by snow-cloud riming at the expense of graupel-cloud riming and by vapor deposition on ice crystals at the expense of ice-cloud riming.

In accordance with Glassmeier and Lohmann (2016), Saleeby and Cotton (2013), and Muhlbauer et al. (2010), we thus observe a compensation between the liquid- and mixed-phase as well as between the mixed- and ice-phase pathways to precipitation formation for aerosol-induced increases in glaciation. The “externally constrained” buffering observed here needs to be distinguished from the “statistical” buffering discussed by Glassmeier and Lohmann (2016). In the latter case, buffering is not required to meet an external constraint but occurs on a statistical basis because compensating responses to aerosol perturbations are likely to be found when a multitude of processes are affected. In both cases, buffering is implemented by compensating responses to an aerosol perturbation, but the underlying causes are different.

In view of our budget analysis, the decreasing sensitivity to aerosols with increasing precipitation efficiency

discussed by Miltenberger et al. (2015), Xue et al. (2013), and Geresdi et al. (2017) can be explained as follows: Disregarding effects on glaciation and given an aerosol-independent condensation rate, aerosols can only affect precipitation production by changing the degree of hydrometeor evaporation. Aerosol can affect evaporation by redistributing the total hydrometeor mixing ratio $M_{cl+ci+pr}$ between the different hydrometeor categories because different hydrometeor types feature different fall velocities. The partitioning of the total hydrometeor mixing ratio between nonsedimenting cloud water M_{cl} and the sedimenting precipitation hydrometeors M_{ci+pr} in particular controls evaporation and total precipitation as well as the spillover. The importance of evaporation decreases with increasingly complete conversion of cloud water into precipitation hydrometeors (i.e., precipitation efficiency).

In terms of the interpretation of the precipitation susceptibility concept, the constrained total precipitation production excludes the traditional view that precipitation susceptibility quantifies the strength of precipitation production that changes with changes in N_{cl} along the lines of Albrecht (1989). Our analysis finds that the total precipitation susceptibility is dominated by adjustments, which is consistent given that the steady-state condition corresponds to a maximally adjusted state. This indicates that precipitation susceptibility $d\ln M_{ci+pr}/d\ln N_{cl}$ can be interpreted as a quantification of the redistribution between M_{ci+pr} and M_{cl} that corresponds to a cloud water adjustment $d\ln M_{cl}/d\ln N_{cl}$.

It is interesting to discuss the applicability of the traditional as opposed to the fully adjusted, or steady-state, perspective on precipitation susceptibility. Although the atmosphere is constantly changing, approximate steady-state situations are possible when the time scale at which the atmospheric boundary conditions change is slow as compared to the thermodynamic and microphysical adjustment time scale. Orographic clouds as discussed in this study are one such example because their lifetime can be much longer than the time that individual air parcels spent in the cloud. Stratocumulus clouds are another example (Bretherton et al. 2010). The crucial difference between these two examples is that updraft and condensation in stratocumulus clouds are not aerosol independent. Precipitation formation in stratocumulus thus lacks the balance constraint discussed for orographic clouds. As discussed in the context of Eqs. (3) and (2), the traditional, process-focused perspective on susceptibilities applies on short time scales after a perturbation or change in the atmospheric boundary conditions.

In a fully adjusted situation, precipitation susceptibility can nevertheless be related to the process rates.

In a steady-state cloud, the distribution of total hydrometeor mixing ratio $M_{\text{cl}+\text{ci}+\text{pr}}$ into the different hydrometeor categories does not change with time. For each category, sources and sink thus need to compensate, such that an aerosol-induced redistribution of precipitation formation pathways corresponds to a redistribution of $M_{\text{cl}+\text{ci}+\text{pr}}$ between categories. We formalize this relationship between the redistributions of $M_{\text{cl}+\text{ci}+\text{pr}}$ (i.e., susceptibilities) and the redistribution of precipitation formation pathways (i.e., microphysical rates) by implicit derivation [Eq. (16)]. This relationship implies signs for partial precipitation susceptibilities that are counterintuitive based on the traditional interpretation (e.g., $\partial \ln M_{\text{ci}+\text{pr}} / \partial \ln N_{\text{cl}}|_{M_{\text{cl}}} > 0$). Their explanation instead requires taking into account feedbacks that lead to the redistribution of the total hydrometeor mixing ratio: A droplet-number-induced decrease of the autoconversion rate requires accretion to increase for a reequilibration of the budget. For a fixed cloud water mixing ratio, the precipitation mixing ratio has to increase to achieve an increase as accretion is largely independent of droplet number.

In summary, we find the following picture of aerosol–cloud–precipitation interactions in completely adjusted, externally constrained systems: An increase in N_{cl} reduces autoconversion. This implies that a larger fraction of the total hydrometeor mixing ratio $M_{\text{cl}+\text{ci}+\text{pr}}$ resides in the droplet instead of the precipitation category and leads to such an increase in accretion that compensates for the decrease in autoconversion. For the warm cloud, we find a precipitation susceptibility of approximately -0.25 for this process. In the weakly glaciated part of the mixed-phase cloud, the redistribution leads to an absolutely larger precipitation susceptibility of approximately -0.5 because ice-phase hydrometeors are more effective than rain in producing $M_{\text{ci}+\text{pr}}$. This additional ice-phase adjustment enhances the liquid adjustment, while aerosol effects on the warm and cold precipitation processes compensate each other. The strongly glaciated part of the mixed-phase cloud is controlled by aerosol-induced changes in total diffusional vapor deposition and is thus not susceptible to changes in N_{cl} . Our discussion illustrates that complex cloud systems governed by feedbacks cannot be explained from intuitive arguments based on individual processes alone. Instead, systemwide arguments, for example based on external constraints as shown here, are required.

Acknowledgments. We thank Annette Miltenberger for sharing her experiences with the two-dimensional setup and Ulrich Blahak and Axel Seifert for providing the implementation of the cloud microphysics scheme. Nadja

Herger and Fabiola Ramelli are gratefully acknowledged for their involvement in earlier approaches to orographic precipitation susceptibilities. We also thank three anonymous reviewers for their thoughtful comments that helped to clarify the manuscript. This work was funded by the ETH-domain CCES project OPTIWARES (41-02).

APPENDIX

List of Symbols and Acronyms

$\langle \cdot \rangle$	Spatial average or normalized sum along a trajectory
\cdot_{ci}	Index denoting cloud ice category in SB
\cdot_{cl}	Index denoting cloud droplet category in SB
\cdot_{prg}	Index denoting graupel category in SB
\cdot_{pr}	Index denoting precipitation-size hydrometeor categories in SB (=prl + prs + prg)
\cdot_{prl}	Index denoting rain category in SB
\cdot_{prs}	Index denoting snow category in SB
\cdot_{v}	Index denoting water vapor
\cdot_{x+y}	Index denoting sum of two variables (= $\cdot_x + \cdot_y$)
θ_e	Equivalent potential temperature
acc	Mass accretion rate
act	Mass rate of cloud droplet activation
aut	Mass autoconversion rate
B_{cl}	Budget of M_{cl}
BC	Black carbon aerosol
CCN	Cloud condensation nuclei
coag	Total mass rate of coagulation (=aut + acc + rim)
cond	Mass condensation rate
diff	Total mass rate of vapor deposition in ice-phase hydrometeors (= $i\text{-diff} + g\text{-diff} + s\text{-diff}$)
DU	Dust aerosol
evp	Mass evaporation rate
f_N	Fractional contribution of polluted number concentration to aerosol condition
f_M	Fractional contribution of polluted mass concentration to aerosol condition
f_{SU}	Fractional contribution of sulfate to sulfate-coated dust aerosol
freez	Mass rate of droplet freezing
gc-rim	Mass rate of graupel–droplet riming
g-diff	Mass rate of vapor deposition on graupel
ic-rim	Mass rate of ice–droplet riming
i-diff	Mass rate of vapor deposition on cloud ice
INP	Ice nucleation particle
LWP	Liquid water path
$M_{\text{ci}+\text{pr}}$	Precipitation mixing ratio (i.e., mixing ratio in sedimenting hydrometeors categories)

M_{cl}	Cloud water mixing ratio (i.e., mixing ratio in cloud droplet category)
$M_{cl+ci+pr}$	Total hydrometeor mixing ratio
M_{ci+pr}	Prod production rate of M_{ci+pr}
M_v sink	Depletion rate of M_v
M_x	Mixing ratio of hydrometeors in category x
melt	Mass rate of droplet melting
N_x	Number of hydrometeors in category x
OC	Organic aerosol
r	Mass rate of change of a microphysical process
R	Rain rate
R_{glac}	Fraction of total hydrometeor mixing ratio $M_{cl+ci+pr}$ in ice, snow, or graupel category of SB
R_{pr}	Fraction of total hydrometeor mixing ratio $M_{cl+ci+pr}$ in rain, snow, or graupel category of SB
rim	Total mass rate of M_{cl} riming (=ic-rim + gc-rim + sc-rim)
s	Total precipitation susceptibility
S	Saturation ratio
s_x	Partial precipitation susceptibility with respect to x
sc-rim	Mass rate of snow–droplet riming
s -diff	Mass rate of vapor deposition on snow
SO ₄	Sulfate aerosol
w	Vertical velocity
WBF	Wegener–Bergeron–Findeisen

REFERENCES

- Albrecht, B. A., 1989: Aerosols, cloud microphysics, and fractional cloudiness. *Science*, **245**, 1227–1230, <https://doi.org/10.1126/science.245.4923.1227>.
- Baldauf, M., A. Seifert, J. Forstner, D. Majewski, and M. Raschendorfer, 2011: Operational convective-scale numerical weather prediction with the COSMO model: Description and sensitivities. *Mon. Wea. Rev.*, **139**, 3887–3905, <https://doi.org/10.1175/MWR-D-10-05013.1>.
- Bangert, M., C. Kottmeier, B. Vogel, and H. Vogel, 2011: Regional scale effects of the aerosol cloud interaction simulated with an online coupled comprehensive chemistry model. *Atmos. Chem. Phys.*, **11**, 4411–4423, <https://doi.org/10.5194/acp-11-4411-2011>.
- , and Coauthors, 2012: Saharan dust event impact on cloud formation and radiation over western Europe. *Atmos. Chem. Phys.*, **12**, 4045–4063, <https://doi.org/10.5194/acp-12-4045-2012>.
- Barahona, D., R. E. L. West, P. Stier, S. Romakkaniemi, H. Kokkola, and A. Nenes, 2010: Comprehensively accounting for the effect of giant CCN in cloud activation parameterizations. *Atmos. Chem. Phys.*, **10**, 2467–2473, <https://doi.org/10.5194/acp-10-2467-2010>.
- Bergeron, T., 1935: On the physics of cloud and precipitation. *Proceedings of the Fifth Assembly of the International Union of Geodesy and Geophysics*, Vol. 2, International Union of Geodesy and Geophysics, 156–178.
- Borys, R. D., D. H. Lowenthal, S. A. Cohen, and W. O. J. Brown, 2003: Mountaintop and radar measurements of anthropogenic aerosol effects on snow growth and snowfall rate. *Geophys. Res. Lett.*, **30**, 1538, <https://doi.org/10.1029/2002GL016855>.
- Bretherton, C. S., J. Uchida, and T. N. Blossey, 2010: Slow manifolds and multiple equilibria in stratocumulus-capped boundary layers. *J. Adv. Model. Earth Syst.*, **2** (14), <https://doi.org/10.3894/JAMES.2010.2.14>.
- Chu, X., B. Geerts, L. Xue, and B. Pokharel, 2017: A case study of cloud radar observations and large eddy simulations of shallow stratiform orographic cloud, and the impact of glaciogenic seeding. *J. Appl. Meteor. Climatol.*, **56**, 1285–1304, <https://doi.org/10.1175/JAMC-D-16-0364.1>.
- Cotton, W. R., and R. A. Anthes, 1992: *Storm and Cloud Dynamics*. Elsevier, 883 pp.
- Cozic, J., and Coauthors, 2008: Chemical composition of free tropospheric aerosol for PM1 and coarse mode at the high alpine site Jungfraujoch. *Atmos. Chem. Phys.*, **8**, 407–423, <https://doi.org/10.5194/acp-8-407-2008>.
- Dadashazar, H., and Coauthors, 2017: Relationships between giant sea salt particles and clouds inferred from aircraft physicochemical data. *J. Geophys. Res. Atmos.*, **122**, 3421–3434, <https://doi.org/10.1002/2016JD026019>.
- Duong, H. T., A. Sorooshian, and G. Feingold, 2011: Investigating potential biases in observed and modeled metrics of aerosol–cloud–precipitation interactions. *Atmos. Chem. Phys.*, **11**, 4027–4037, <https://doi.org/10.5194/acp-11-4027-2011>.
- Feingold, G., and H. Siebert, 2009: Cloud–aerosol interactions from the micro to the cloud scale. *Clouds in the Perturbed Climate System: Their Relationship to Energy Balance, Atmospheric Dynamics, and Precipitation*, J. Heintzenberg, and R. J. Charlson, Eds., MIT Press, 319–338.
- , A. McComiskey, D. Rosenfeld, and A. Sorooshian, 2013: On the relationship between cloud contact time and precipitation susceptibility to aerosol. *J. Geophys. Res. Atmos.*, **118**, 10 544–10 554, <https://doi.org/10.1002/jgrd.50819>.
- Findeisen, W., 1938: Die kolloidmeteorologischen Vorgänge bei der Niederschlagsbildung (Colloidal meteorological processes in the formation of precipitation). *Meteor. Z.*, **55**, 121–133.
- Fountoukis, C., and A. Nenes, 2005: Continued development of a cloud droplet formation parameterization for global climate models. *J. Geophys. Res.*, **110**, D11212, <https://doi.org/10.1029/2004JD005591>.
- Geresdi, I., L. Xue, and R. Rasmussen, 2017: Evaluation of orographic cloud seeding using a bin microphysics scheme: Two-dimensional approach. *J. Appl. Meteor. Climatol.*, **56**, 1443–1462, <https://doi.org/10.1175/JAMC-D-16-0045.1>.
- Glassmeier, F., and U. Lohmann, 2016: Constraining precipitation susceptibility of warm-, ice-, and mixed-phase clouds with microphysical equations. *J. Atmos. Sci.*, **73**, 5003–5023, <https://doi.org/10.1175/JAS-D-16-0008.1>.
- , A. Possner, B. Vogel, H. Vogle, and U. Lohmann, 2017: A comparison of two chemistry and aerosol schemes on the regional scale and resulting impact on radiative properties and liquid- and ice-phase aerosol–cloud interactions. *Atmos. Chem. Phys.*, **17**, 8651–8680, <https://doi.org/10.5194/acp-17-8651-2017>.
- Hande, L. B., C. Hoose, and C. Barthlott, 2017: Aerosol- and droplet-dependent contact freezing: Parameterization development and case study. *J. Atmos. Sci.*, **74**, 2229–2245, <https://doi.org/10.1175/JAS-D-16-0313.1>.
- Jiang, H., G. Feingold, and A. Sorooshian, 2010: Effect of aerosol on the susceptibility and efficiency of precipitation in warm

- trade cumulus clouds. *J. Atmos. Sci.*, **67**, 3525–3540, <https://doi.org/10.1175/2010JAS3484.1>.
- Jiang, Q., and R. B. Smith, 2003: Cloud timescales and orographic precipitation. *J. Atmos. Sci.*, **60**, 1543–1559, <https://doi.org/10.1175/2995.1>.
- Jung, E., B. A. Albrecht, A. Sorooshian, P. Zuidema, and H. H. Jonsson, 2016: Precipitation susceptibility in marine stratocumulus and shallow cumulus from airborne measurements. *Atmos. Chem. Phys.*, **16**, 11 395–11 413, <https://doi.org/10.5194/acp-16-11395-2016>.
- Kanji, Z. A., L. A. Ladino, H. Wex, Y. Boose, M. Burkert-Kohn, D. J. Cziczo, and M. Krämer, 2017: Overview of ice nucleating particles. *Ice Formation and Evolution in Clouds and Precipitation: Measurement and Modeling Challenges*, *Meteor. Monogr.*, No. 58, Amer. Meteor. Soc., 1–33, <https://doi.org/10.1175/AMSMONOGRAPHS-D-16-0006.1>.
- Köhler, H., 1936: The nucleus in and the growth of hygroscopic droplets. *Trans. Faraday Soc.*, **32**, 1152–1161, <https://doi.org/10.1039/TF9363201152>.
- Korolev, A., 2007: Limitations of the Wegener–Bergeron–Findeisen mechanism in the evolution of mixed-phase clouds. *J. Atmos. Sci.*, **64**, 3372–3375, <https://doi.org/10.1175/JAS4035.1>.
- Miltenberger, A. K., A. Seifert, H. Joos, and H. Wernli, 2015: A scaling relation for warm-phase orographic precipitation: A Lagrangian analysis for 2D mountains. *Quart. J. Roy. Meteor. Soc.*, **141**, 2185–2198, <https://doi.org/10.1002/qj.2514>.
- Muhlbauer, A., T. Hashino, L. Xue, A. Teller, U. Lohmann, R. M. Rasmussen, I. Geresdi, and Z. Pan, 2010: Intercomparison of aerosol-cloud-precipitation interactions in stratiform orographic mixed-phase clouds. *Atmos. Chem. Phys.*, **10**, 8173–8196, <https://doi.org/10.5194/acp-10-8173-2010>.
- Nenes, A., and J. H. Seinfeld, 2003: Parameterization of cloud droplet formation in global models. *J. Geophys. Res.*, **108**, 4415, <https://doi.org/10.1029/2002JD002911>.
- Noppel, H., U. Blahak, A. Seifert, and K. D. Beheng, 2010: Simulations of a hailstorm and the impact of CCN using an advanced two-moment cloud microphysical scheme. *Atmos. Res.*, **96**, 286–301, <https://doi.org/10.1016/j.atmosres.2009.09.008>.
- Phillips, V. T. J., P. J. DeMott, and C. Andronache, 2008: An empirical parameterization of heterogeneous ice nucleation for multiple chemical species of aerosol. *J. Atmos. Sci.*, **65**, 2757–2783, <https://doi.org/10.1175/2007JAS2546.1>.
- Saleeby, S. M., and W. R. Cotton, 2013: Aerosol impacts on the microphysical growth processes in orographic snowfall. *J. Appl. Meteor. Climatol.*, **52**, 834–852, <https://doi.org/10.1175/JAMC-D-12-0193.1>.
- , —, D. Lowenthal, R. D. Borys, and M. A. Wetzel, 2009: Influence of cloud condensation nuclei on orographic snowfall. *J. Appl. Meteor. Climatol.*, **48**, 903–922, <https://doi.org/10.1175/2008JAMC1989.1>.
- , —, and J. D. Fuller, 2011: The cumulative impact of cloud droplet nucleating aerosols on orographic snowfall in Colorado. *J. Appl. Meteor. Climatol.*, **50**, 604–625, <https://doi.org/10.1175/2010JAMC2594.1>.
- Seifert, A., and K. D. Beheng, 2006: A two-moment cloud microphysics parameterization for mixed-phase clouds. Part I: Model description. *Meteor. Atmos. Phys.*, **92**, 45–66, <https://doi.org/10.1007/s00703-005-0112-4>.
- Sorooshian, A., G. Feingold, M. D. Lebsock, H. Jiang, and G. L. Stephens, 2009: On the precipitation susceptibility of clouds to aerosol perturbations. *Geophys. Res. Lett.*, **36**, L13803, <https://doi.org/10.1029/2009GL038993>.
- , —, —, —, and —, 2010: Deconstructing the precipitation susceptibility construct: Improving methodology for aerosol-cloud precipitation studies. *J. Geophys. Res.*, **115**, D17201, <https://doi.org/10.1029/2009JD013426>.
- Stevens, B., and G. Feingold, 2009: Untangling aerosol effects on clouds and precipitation in a buffered system. *Nature*, **461**, 607–613, <https://doi.org/10.1038/nature08281>.
- Teraï, C. R., R. Wood, D. C. Leon, and P. Zuidema, 2012: Does precipitation susceptibility vary with increasing cloud thickness in marine stratocumulus? *Atmos. Chem. Phys.*, **12**, 4567–4583, <https://doi.org/10.5194/acp-12-4567-2012>.
- Vogel, B., H. Vogel, D. Bäumer, M. Bangert, K. Lundgren, R. Rinke, and T. Stanelle, 2009: The comprehensive model system COSMO-ART—Radiative impact of aerosol on the state of the atmosphere on the regional scale. *Atmos. Chem. Phys.*, **9**, 8661–8680, <https://doi.org/10.5194/acp-9-8661-2009>.
- Wacker, U., 1995: Competition of precipitation particles in a model with parameterized cloud microphysics. *J. Atmos. Sci.*, **52**, 2577–2589, [https://doi.org/10.1175/1520-0469\(1995\)052<2577:COPPIA>2.0.CO;2](https://doi.org/10.1175/1520-0469(1995)052<2577:COPPIA>2.0.CO;2).
- , 2006: Nonlinear effects in a conceptual multilayer cloud model. *Nonlinear Processes Geophys.*, **13**, 99–107, <https://doi.org/10.5194/npg-13-99-2006>.
- Wegener, A., 1911: *Thermodynamik der Atmosphäre*. Johann Ambrosius Barth, 331 pp.
- Weingartner, E., S. Nyeki, and U. Baltensperger, 1999: Seasonal and diurnal variation of aerosol size distributions ($10 < D < 750$ nm) at a high-alpine site (Jungfraujoch 3580 m ASL). *J. Geophys. Res.*, **104**, 26 809–26 820, <https://doi.org/10.1029/1999JD900170>.
- Wood, R., T. L. Kubar, and D. L. Hartmann, 2009: Understanding the importance of microphysics and macrophysics for warm rain in marine low clouds. Part II: Heuristic models of rain formation. *J. Atmos. Sci.*, **66**, 2973–2990, <https://doi.org/10.1175/2009JAS3072.1>.
- Xue, L., and Coauthors, 2013: Implementation of a silver iodide cloud-seeding parameterization in WRF. Part I: Model description and idealized 2D sensitivity tests. *J. Appl. Meteor. Climatol.*, **52**, 1433–1457, <https://doi.org/10.1175/JAMC-D-12-0148.1>.